Experimental stress state-dependent void nucleation behavior for advanced high strength steels

N. Pathak, J. Adrien, C. Butcher, E. Maire, M. Worswick

Experimental stress state-dependent void nucleation behavior for advanced high strength steels

N. Pathak[a,*], J. Adrien[b], C. Butcher[a], E. Maire[b], M. Worswick[a]

[a] Department of Mechanical and Mechatronics Engineering, University of Waterloo, Waterloo, ON, Canada
[b] GEMPPM, INSA de Lyon, Lyon, Villeurbanne, France

ARTICLE INFO

Keywords:
AHSS
Void nucleation
Stress-triaxiality
Lode parameter
Damage

ABSTRACT

The influence of microstructure and stress state, as defined by the stress triaxiality and Lode parameter, on micro-void nucleation was evaluated experimentally for two 800 MPa Advanced High Strength Steels (AHSS), one a Complex-Phase CP800 alloy, with a ferritic-bainitic microstructure, and the other a Dual-Phase DP780 ferritic-martensitic steel. Four plane stress specimen geometries (simple shear, hole tension, v-bend and biaxial Nakazima) were adopted, providing stress triaxiality and Lode parameter values ranging from in-plane shear to biaxial tension under approximately constant stress states until failure. This approach facilitated determination of the relationship between void nucleation and macroscopic stress state. Damage histories were developed from interrupted samples using 3D micro-tomography and quantitative stereology measurement of void nucleation paired with *in situ* digital image correlation (DIC) strain measurements during the mechanical testing. The trends in damage evolution are strongly linked to the stress state, with very little void nucleation under shear deformation but extensive void damage under biaxial tension for both materials. A dependency of the nucleation rate on Lode parameter was also demonstrated. A higher rate of damage accumulation was observed for the DP780 steel compared to damage in the CP800 steel for all loading conditions highlighting the strong influence of initial microstructure. An analytical framework is proposed to obtain the local stress-state and equivalent plastic strain history from direction integration of the measured DIC strain histories, using a measured hardening law and assumed anisotropic yield function (Yld91) to develop the link between nucleation and the macroscopic stress state. A stress-state dependent nucleation model is proposed by introducing a nucleation strain surface as a function of stress-triaxiality and Lode parameter using a modified form of the strain-based Chu and Needleman nucleation criterion.

1. Introduction

Dual-phase (DP) steels, have gained rapid acceptance in automotive industries by producing thinner-gauge and lighter components while retaining good formability and high strength. New variants of DP steels rely upon a multi-phase microstructure which consists of a high-strength martensitic islands embedded in a soft ferritic matrix to provide an excellent combination of strength and ductility [1]. However, one of the major concerns associated with DP steels is that they can be susceptible to abrupt cracking during sheared edge stretching operations [2,3]. As an alternative, ferritic-bainitic complex phase (CP) steels have been reported to provide improved edge flangeability [4–6]. Due to the presence of a significant fraction of martensite in the DP steel, a higher strength-differential is created within the ferrite matrix, resulting in an accelerated damage evolution compared to the CP steel with a less strength difference between the bainite and ferrite phases [7]. Consequently, this disparity in microstructure leads to a lower resistance to sheared edge cracking for the DP steel compared to the CP steel. For steel producers seeking to optimize the microstructures of AHSS to improve performance in industrial forming operations, there is considerable interest in further understanding the influence of microstructure on damage evolution and subsequent failure.

The fracture mechanism of ductile materials generally involves the nucleation, growth and coalescence of microscopic voids [8]. During plastic deformation, voids nucleate and grow until they coalescence with neighboring voids to create micro-cracks [9]. Extensive work has been conducted to study damage evolution in the DP steels [10–13]. Avramovic-Cingara et al. [10] conducted optical microscopy and scanning electron microscopy to quantify damage during tensile loading. X-ray tomography techniques have been used to observe damage evolution in DP steel by the 3D reconstruction of 2D images [11–13]. Kahziz et al. [14] conducted laminography to characterize damage during deformation of a DP600 sheared edge. Pathak et al. [7] conducted void measurements on the CP800 and DP780 steels using optical microscopy

* Corresponding author.
E-mail address: n3pathak@uwaterloo.ca (N. Pathak).

https://doi.org/10.1016/j.ijmecsci.2020.105661

and DIC strain measurement. To-date, the studies on 3D quantification of void evolution have not been reported for the ferritic-baintic steels to the authors' knowledge. Moreover, most of the literatures available on AHSS investigated damage mechanism under uniaxial tension.

The stress-state is often defined in terms of the stress triaxiality and the Lode parameter in models of fracture. The influence of stress-triaxiality on damage evolution has been inferred experimentally and analytically [11,15,16]. Landron et al. [11] quantified the nucleation of voids for two different specimens: tensile and higher triaxiality notch specimens and observed the influence of stress state on damage evolution. Hancock and Mackenzie [17] conducted experiments on smooth and notched round bars and observed increasing ductility with decreasing stress triaxiality in three different low-alloy steels. Barsoum and Faleskog [18] observed experimentally that the rupture mechanism shifts from internal necking at high stress triaxiality to internal shear localization at low stress triaxiality. Needleman [19] studied the effect of different loading conditions on nucleation and correlated the onset of nucleation to stress triaxiality level. Xu and Needleman [20] reported that the stress triaxiality determines whether decohesion or cracking occurs first. Recently, Yu [21] performed 3D unit cell simulation to investigate the effect of stress triaxiality and Lode angle on nucleation at the particle-matrix interface. The results reveal that both the stress triaxiality and Lode angle parameter affects the nucleation process.

There is a wide variety of models available to capture void growth and coalescence as a function of stress state and these have been successfully implemented in finite element models to simulate the ductile fracture process [9,22,23]. In contrast, studies on void nucleation are less common due to the complexity of the required experimental measurements and strong dependence on microstructure. Void nucleation occurs at the inclusions and second-phase particles due to the cracking or debonding from the matrix material [10,24]. An elongated particle is more susceptible to debonding if aligned transverse to the principal loading direction and exhibits cracking if aligned in the loading direction [19]. A larger particle nucleates earlier due to the presence a large interface, more surface internal defects, and often are irregularly shaped [25]. Ultimately, whether a particle will crack or debond depends on the size, shape, distribution, strength of the particle and interface [19,26–29]. Overall, void nucleation is a complex process which is difficult to predict. Moreover, the void nucleation in AHSS steels was found to be more complex than in homogeneous materials, such as conventional steels and mild steels or aluminum, because of their multiphase microstructure [10,24]. The potential nucleation sites in a multi-phase microstructure are randomly distributed within or around different phases and particles [7,30–32]. The modeling of nucleation mechanism would require capturing deformation of each particle and phases and their subsequent cracking and debonding.

Void nucleation can be modeled using an energy criterion [25,33], and be stress-controlled [34,35] or strain-controlled [36]. The void nucleation based on critical stress conditions have more physical relevance, but are difficult to implement due to intricacies of the void nucleation mechanism arising from the microstructure of a material. As an alternative approach, continuum void nucleation models have been developed. Chu and Needleman [36] proposed a continuum approach to model void nucleation and the strain-controlled Chu and Needleman model has been extensively used by the researchers to predict void nucleation in aluminum and steels [37,38]. Butcher et al. [39,40] successfully implemented a stress-based nucleation rule to predict void nucleation in aluminum and AHSS grade. Despite overwhelming evidence that damage evolution is sensitive to the stress state [11,15], the effect of stress state on void nucleation has received limited attention to-date. Landron et al. [11] formulated the nucleation of voids as a function of stress triaxiality by modifying the Argon [41] criterion. However, the influence of Lode parameter has not been considered in the nucleation models. It is interesting that extensive work has been done to account for the influence of stress-state on void growth and coalescence, yet the effect of stress state on nucleation rate has been largely overlooked.

The first objective of the current work is to determine the influence of loading condition (stress state) on void nucleation and develop a nucleation rule as a function of stress triaxiality and Lode parameter for two different AHSS grades: DP780 and CP800 steels. The second objective is to consider the effect of microstructure on nucleation rate and for this, two different microstructure-types, ferritic-martensitic DP780 and ferritic-bainitic CP800 steels, are considered. The stress state is varied by considering four key experiments to characterize the strain to fracture for simple shear, uniaxial tension, plane strain tension and equi-biaxial tension. An attempt was made to select experiments that minimize necking and provide a nearly constant stress state throughout the experiments; these are the hemispherical dome test, hole tension test, v-bend test and a shear test. An analytical framework is presented to experimentally estimate the local stress and strain history at the fracture location using the Swift hardening law, Yld91 [42] anisotropic yield function and measured strain components using digital image correlation (DIC). A series of interrupted tests using stereoscopic DIC was conducted to determine the local strain field and correlate the equivalent strain with void measurements using 3D tomography. A specimen was extracted from the maximum deformed region of each interrupted sample and an *ex-situ* 3D tomography was conducted on each specimen to quantify voids at each level of deformation and for the different proportional loading conditions. The experimental investigation of the influence of stress state on void nucleation was used to develop an experimental stress state dependent nucleation rule for each material. A modified strain-controlled Chu and Needleman [36] nucleation criterion is proposed to account for the stress states by introducing a nucleation strain surface as a function of stress triaxiality and Lode parameter.

2. Experiment

2.1. Material characterization

The mechanical properties of the two materials investigated herein, CP800 and DP780 steels, have been studied by the authors in the past studies [6]. The mechanical properties of the two steels are listed in Table 1: yield strength (*YS*), ultimate tensile strength (*UTS*), percentage total elongation (% *TE*), strain hardening exponent (*n*) and Lankford coefficients (*r*). The UTS experiments in the current work were aligned with the TD.

2.2. Biaxial stress state experiments

A stress state corresponding to biaxial tension was obtained by conducting a Nakazima hemispherical dome test [43]. The experiment set up consists of a die, a blank holder and a punch of diameter 101.6 mm, with a die-entry radius of 6.35 mm. The biaxial specimen (shown in Fig. 1) consisted of a 200 mm by 200 mm sheet blank that was clamped prior to punch movement using a blank holder force of 650 kN. A punch speed of 0.25 mm/s was used to achieve a quasi-static strain rate. The test and tooling conforms to ISO12004-2, aside from using the lower

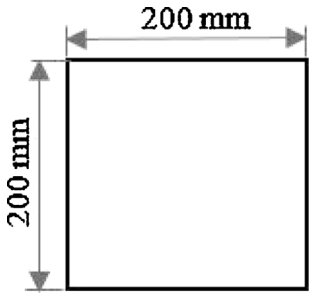

Fig. 1. Specimen geometry used for the biaxial test. All units are in mm.

Table 1
Mechanical properties in the rolling direction (RD), transverse direction (TD) and diagonal direction (DD) of the CP and DP steels. The standard deviation after three tests is indicated in the bracket [6].

Material	Thickness (mm)	Direction	YS (MPa)	UTS (MPa)	TE (%)	*n (5-UE%)*	*R*
CP800	2.90	RD	710 (6)	810 (3)	19.6 (1.7)	0.08 (0.00)	0.70 (0.04)
		TD	788 (5)	850 (5)	18.8 (1.0)	0.06 (0.00)	0.95 (0.04)
		DD	726 (8)	800 (5)	20.5 (2.0)	0.07 (0.00)	1.33 (0.03)
DP780	1.56	RD	509 (8)	800 (6)	22.8 (2.2)	0.16 (0.00)	0.72 (0.02)
		TD	522 (4)	806 (5)	21.6 (1.8)	0.15 (0.00)	0.92 (0.03)
		DD	533 (6)	815 (8)	25.5 (1.8)	0.15 (0.00)	0.98 (0.01)

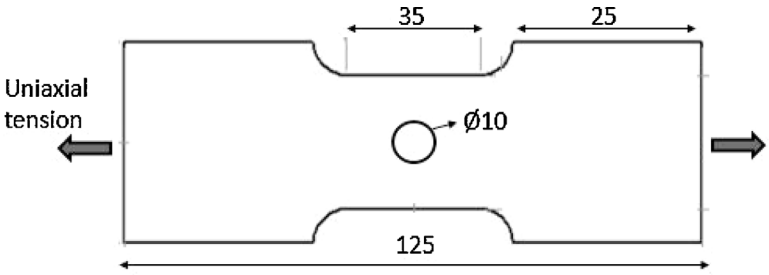

Fig. 2. Specimen geometry used for the DP780 hole tension test. All units are in mm.

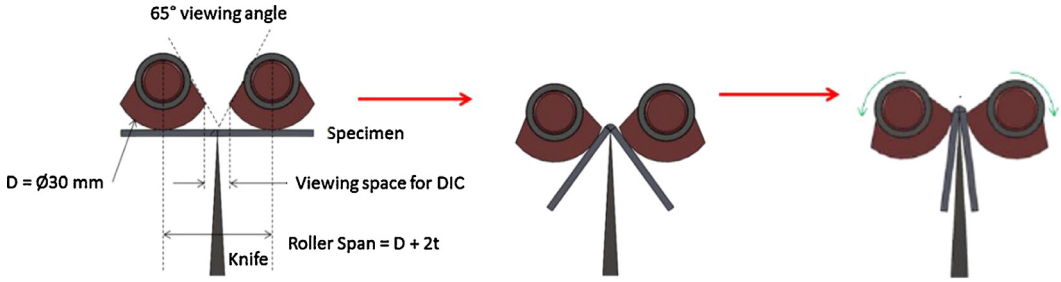

Fig. 3. Concept of Cheong et al. [46] for the tight radius v-bend process.

punch speed of 0.25 mm/s which is less than the lower limit in the standard of 0.5 mm/s. The punch force and displacement was recorded during testing while stereo DIC was used to measure the strain field using a camera frame rate of 6 images per second. The DIC software was provided by Correlated Solutions Inc. For post-processing of the captured images, the DIC images were analyzed at a resolution of 0.03 mm/pixel and the logarithmic strain was computed using DIC step and filter sizes of 3 and 6 pixels, respectively. To quantify the influence of the strain filter size and step size in the DIC post-processing, the Virtual Strain Gauge Length (VSGL) was calculated in the equation described below:

$$\text{VSGL} = \text{Filtersize} \times \text{Resolution of the area of interest} \times \text{Step size} \quad (1)$$

With the current DIC setting, the value of VSGL obtained is 0.5 mm.

2.3. Hole tension experiment

Ebnoether and Mohr (2013) [44] demonstrated that stress triaxiality in a conventional tensile specimen can vary from 0.33 at onset of necking to 0.8 prior to failure. Bao et al. [45] reported that a tensile specimen with a central hole located at its center exhibits approximately uniaxial tension at the intersection of the hole and the transverse symmetry plane (the normal location of failure onset) since deformation of a free edge is one of uniaxial tension. Given this desirable near-constant triaxiality, this test was used in the present work to acquire failure strains corresponding to a uniaxial tension stress state. A tensile specimen with a gauge length of 35 mm was fabricated with a central hole of diameter 10 mm (as indicated in Fig. 2). The width of the ligament on either side of the hole was selected to be four times larger than the sheet thickness for the two materials considered. A 100 kN Instron testing apparatus was used to conduct the tension test at a cross-head displacement of 0.075 mm/s and strain rate corresponding to 0.003 s^{-1}. The strain measurements were recorded during the experiment using stereo DIC at an acquisition rate of 4 images per second. The DIC images were analyzed using a resolution of 0.02 mm/pixel, a filter size and step size of 9 and 3 pixels, respectively, to obtain VSGL of 0.5 mm.

2.4. V-bend experiment

The fracture strain in plane strain tension was characterized by conducting tight radius bending (v-bend) tests, illustrated in Fig. 3. The mechanical arrangement was developed by Cheong et al. [46] and was designed to be compatible with stereographic DIC imaging by keeping the punch stationary and moving the rollers downwards to carry-out the bending. The rollers are chamfered to provide a 65° viewing angle thereby enabling full field DIC of the tensile side of the bend specimen during the entire test. In addition, the bend region remains stationary on the fixed punch and hence enables higher DIC resolution. The 30 mm x 30 mm DP780 specimens and 58 mm x 58 mm CP800 specimens were electric discharge machined (EDM) instead of shearing to avoid edge cracking. A punch with 0.4 mm radius of curvature was used and the 30 mm diameter rollers moved downwards at 20 mm/minute. The rollers were spaced such that the gap between the cylindrical surfaces of the rollers was 2.5 times the thickness of material, in accordance with the VDA 238-100 specification [47]. The post processing of the DIC images was performed at a resolution of 0.01 mm/pixel, a step size of 5 pixels, a subset size of 37and a strain filter size of 10 pixels that corresponding to a virtual strain gauge length of 0.5 mm.

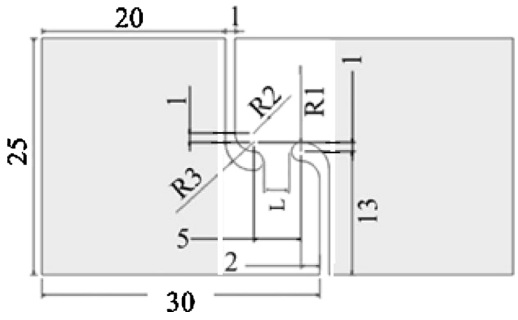

Fig. 4. Shear specimen geometry of Peirs et al. [48]. Gripped region is shaded.

2.5. Simple shear experiment

Simple shear tests performed on CP800 and DP780 steels considered the shear geometry of Peirs et al. [48] as indicated in Fig. 4. A 100 kN MTS Criterion model 45 servo-electric tensile frame was used to perform the tests at a 0.03 mm/s cross-head displacement rate corresponding to an approximate von Mises equivalent strain-rate of 0.01 s^{-1} at the specimen center. The shear tests were performed with the load applied in the diagonal direction of the sheet that results in the principal stresses being aligned with the transverse and rolling directions, as reported by Abedini et al. [49]. DIC imaging was used to record deformation at a rate of 6 frames/s. The post processing was performed using a subset size of 31 pixels, a strain filter size of 7 pixels, and a step size of 3 pixels and at a resolution of 0.15 mm /pixels. A VSGL of 0.3 mm was calculated with the above DIC setting, which is in agreement with the setting suggested by Rahmaan et al. [50].

2.6. X-ray tomography

Tomography specimens of cross-section 500 μm x 500 μm and length 700 μm were extracted from the region of maximum deformation of each interrupted specimen, as discussed in Section 3. The samples were fabricated by grinding to approximately 0.7 mm thickness with a continuous water supply to avoid heating of the sample, followed by cutting to the desired cross-section, using an Accutom precision cutter. Tomographs of the specimens were acquired using the EasyTom system at the MATEIS laboratory in INSA Lyon. The tomograph was operated at 100 kV and 75 μA with a Cu filter to obtain a voxel size of 1 μm. Reconstructed volumes were first median filtered with a radius of two voxels to reduce the noise associated with the scan acquisition. Thresholding was conducted to differentiate the void volume from the steel phase. The edge surface was detected using an ImageJ plugin [51] based on a Sobel edge detector that highlights sharp difference in intensity in 3D binarized volumes. ImageJ 3D volume viewer was used to perform the 3D visualization. In the 3D views of the reconstructed slices presented herein, voids appear in red and the bulk material in white. A similar void measurement technique was used by Landron et al. [52]. To be registered as a void, a set of pixels need to be statistically significant in three dimensions; therefore, voids with the diameter less than twice the voxel size i.e. 2.0 μm were excluded in the analysis. The void quantification was conducted using ImageJ to provide measurements of individual voids within a specimen.

3. Locally proportional loading histories

A key aspect of the ductile fracture experiments was to obtain proportional loading; i.e. a constant strain path and stress state during deformation up to the point of fracture initiation. This section examines the strain paths achieved during testing and also introduces a technique to extract the stress state histories through direct integration of the constitutive laws using only the measured DIC strains at the points of interest.

3.1. Experimental strain paths

The equivalent strain, ε_{eq}, in the DIC software was calculated based on von Mises plasticity theory and plastic volume conservation by integrating Eq. (2),

$$d\varepsilon_{eq} = \frac{2}{\sqrt{3}}\sqrt{\left(d\varepsilon_1^2 + d\varepsilon_2^2 + d\varepsilon_1^2\, d\varepsilon_2^2\right)} \tag{2}$$

Jonas et al. [53] and Shrivastava et al. [54] stated that the rotation of principal strain with respect to the principal stresses must be accounted for simple shear. Butcher and Abedini [55] accounted for misalignment of the principal frames in the calculation of von-Mises work-conjugate equivalent plastic strain for finite shear as a function of the major strain, as

$$\varepsilon_{eq} = \frac{2}{\sqrt{3}}\sinh\varepsilon_1 \tag{3}$$

where ε_1 is a major strain. The equivalent strain for simple shear condition is calculated using Eq. (3) and for the rest of stress states, Eq. (2) is used.

Fig. 5 shows the measured contours of equivalent strain for the different test specimens: biaxial dome, v-bend, hole tension and shear for the CP800 and DP780 steels just prior to failure. Tomography specimens of cross-section, 500 μm x 500 μm, extracted from the maximum deformation region is highlighted in Fig. 5 using a grey colored square for each specimen.

Fig. 6 shows the strain-path for each test geometry extracted from the region of maximum deformation, corresponding to the 0.5 mm regions indicated in Fig. 5, for both materials. The DIC strains were averaged over the square of size 0.50 mm to match the size of the tomography specimens to provide an appropriate macroscopic strain to correlate with void nucleation. The dashed lines plotted in Fig. 6 indicate the theoretical strain paths for an isotropic material with principal strain ratios (slopes) of −1, 0, −0.5 and 1 corresponding to equal-biaxial tension, plane-strain, uniaxial tension and shear respectively. During the shear and v-bend testing, the principal strain path followed is linear and proportional throughout the deformation. The strain path followed during the dome test is biaxial until near failure at which point the path transitions towards plane-strain. Similarly the principal strain ratio obtained from the hole tension test is uniaxial throughout the deformation for the DP780 and deviates to plane-strain for the CP800 steel due to necking or strain localization. Roth and Mohr [56] reported that altering the hole tension specimen geometry (i.e. decreasing hole size) can shift the onset of localization to higher strain, thus, further delay in the onset of necking mayhave been possible in the CP800 experiments by modifying the hole tension specimen geometry. Such modifications were not considered in the current research since the onset of necking is already considerably delayed relative to that seen in a uniaxial tensile specimen.

3.2. Stress integration using DIC-based measured stains

In this section, an analytical approach is presented to calculate local stress using (a) DIC strain measurements, (b) a suitable yield function and (c) an appropriate hardening law. A brief description of the material model is presented, followed by the algorithm to integrate the stress components from the strain measurements.

3.2.1. Material model

In 1991, Barlat [42] proposed a 3D yield function (called Yld91) which can provide a good representation of the variation in the yield stress and *r*-values for steel and aluminum alloys. More advanced yield criteria such as Yld2004 are available, but require more extensive experimental characterization to calibrate the yield function. Consequently, the Yld91 criterion was adopted to model anisotropy of the CP800 and DP780 steels and can be expressed as

$$\sigma = \left(0.5\left(\left|S_1 - S_2\right|^m + \left|S_2 - S_3\right|^m + \left|S_3 - S_1\right|^m\right)\right)^{1/m} \tag{4a}$$

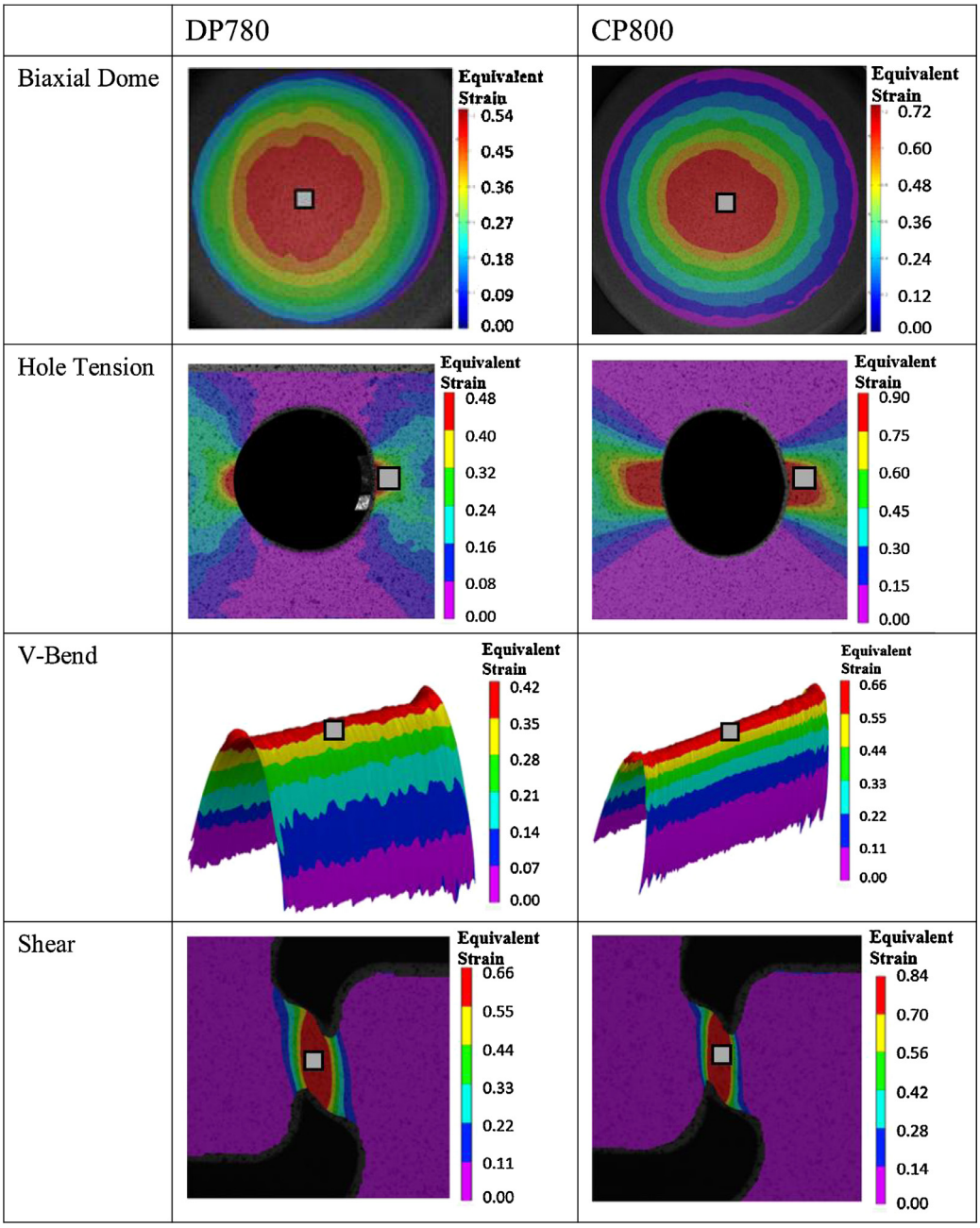

Fig. 5. Measured contours of equivalent strain for the biaxial dome, hole tension, v-bend and shear tests for the (a) CP800 and (b) DP780 steels prior to failure. The location of tomography specimen is highlighted using a square for each specimen.

where m is chosen based on the crystallographic structure. S_1, S_2 and S_3 are eigenvalues of the symmetric transformed stress tensor $\mathbf{S}$

$$\mathbf{S} = \begin{bmatrix} S_{11} & S_{12} & S_{13} \\ S_{12} & S_{22} & S_{23} \\ S_{13} & S_{23} & S_{33} \end{bmatrix} \tag{4b}$$

where

$$S_{11} = \frac{c(\sigma_{xx} - \sigma_{yy}) - b(\sigma_{zz} - \sigma_{xx})}{3} \tag{4c}$$

$$S_{22} = \frac{a(\sigma_{yy} - \sigma_{zz}) - c(\sigma_{xx} - \sigma_{yy})}{3} \tag{4d}$$

$$S_{33} = \frac{b(\sigma_{zz} - \sigma_{xx}) - a(\sigma_{yy} - \sigma_{zz})}{3} \tag{4e}$$

$$S_{12} = h\sigma_{xy} \tag{4f}$$

$$S_{23} = g\sigma_{xz} \tag{4g}$$

$$S_{31} = f\sigma_{yz} \tag{4h}$$

and a, b, c, h, g, f are calibration parameters. In the current work, an equivalent plastic work methodology was implemented to calibrate the Yld91 function for both steels. The plastic work, w^p, was calculated from the tensile test along the rolling, transverse and diagonal directions and the shear test using the following equation.

$$dw^p = \sigma_1 d\varepsilon_1^p + \sigma_2 d\varepsilon_2^p + \sigma_3 d\varepsilon_3^p = \sigma_{eq} d\varepsilon_{eq}^p \tag{5a}$$

$$w^p = \int dw^p \tag{5b}$$

The stress anisotropy is determined, at a given plastic work level, as a ratio of the stress in a particular material orientation divided by the corresponding tensile stress along the rolling direction for the same plastic work. These "stress ratios" are plotted in Fig. 7. A slight variation

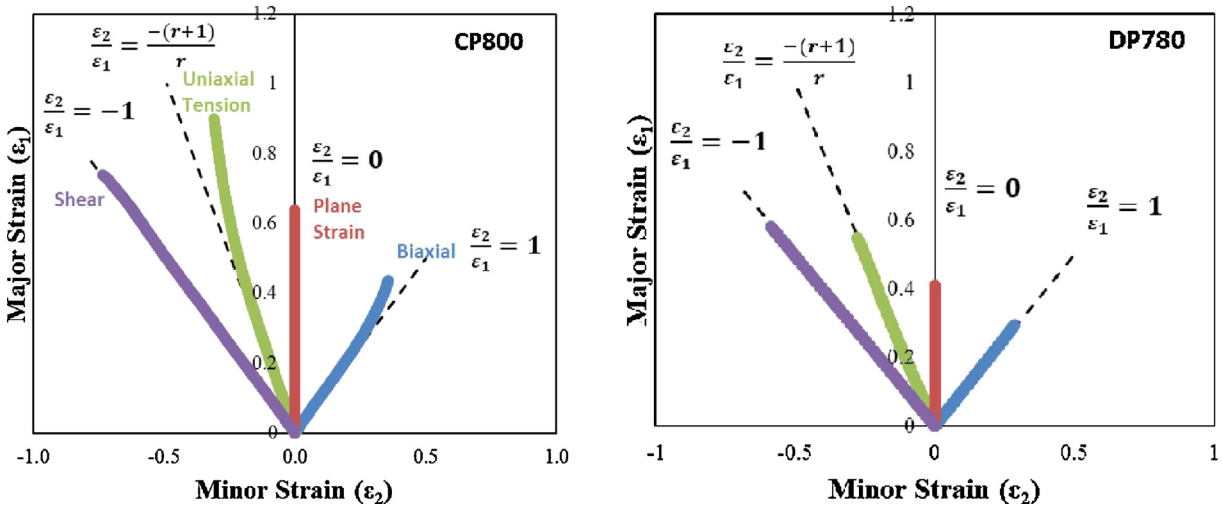

Fig. 6. Major and minor strains paths in the region of maximum deformation subjected to different loading conditions for the (a) CP800 and (b) DP780 steels.

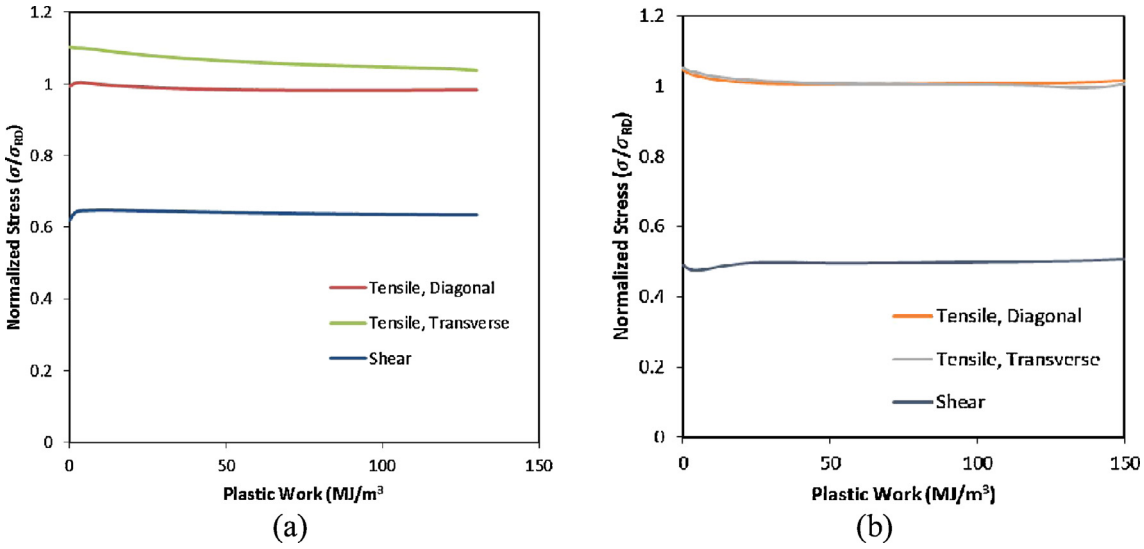

Fig. 7. Stress ratios with respect to rolling direction for (a) CP800 and (b) DP780 materials.

Table 2
Stress-ratios at a plastic work of 55.2 MPa for the tension test along the diagonal and transverse directions and shear test for the CP800 and DP780 steels.

Material	σ_D/σ_R	σ_T/σ_R	τ/σ_R
CP800	0.98	1.08	0.63
DP780	1.00	1.00	0.50

in the values was observed during the deformation, especially near yield point. The values corresponding to the plastic work at UTS in the rolling direction (55.2 MPa) were used in calibration of yield function and are listed in Table 2 for the CP800 and DP780 steels. The *r*-values used in the calibration of yield function are listed in Table 1.

The Yld91 parameters (plane stress assumption) were determined using an optimization approach in which a least squares error minimization was performed to reduce error between the values derived by the yield function and the experimental data. The global optimization MATLAB subroutine based on genetic algorithm, was selected in the current study to perform minimization for the following "*Error*" function:

$$Error = w_\sigma \sum_{i=1}^{t} \left(\left(\frac{\sigma_{model}}{\sigma_{exp}} \right)_i - 1 \right)^2 + w_r \sum_{i=1}^{t} \left(\left(\frac{r_{model}}{r_{exp}} \right)_i - 1 \right)^2 \quad (6)$$

The "exp" and "model" in Eq. (6) represents experimental values and predicted values from the yield function, respectively. w_σ and w_r are weights applied to values of stress and *r*-value, respectively, and *t* is the number of experimental points. A shear constraint, introduced by Abedini [57], was also implemented to enforce normality in the shear regions of anisotropic yield function. An exponent of $m = 6$ is used for both the materials which is recommended value for bcc materials [42] in the anisotropic model, and the resulting coefficients for the yield function are listed in Table 3.

Table 3
The parameters of Yld91 yield function for the CP800 and DP780 steels.

Material	*a*	*b*	*c*	*h*	*g*	*f*
CP800	−0.81	0.85	0.12	1.00	1.00	−1.04
DP780	−1.00	0.60	0.47	1.00	1.00	0.99

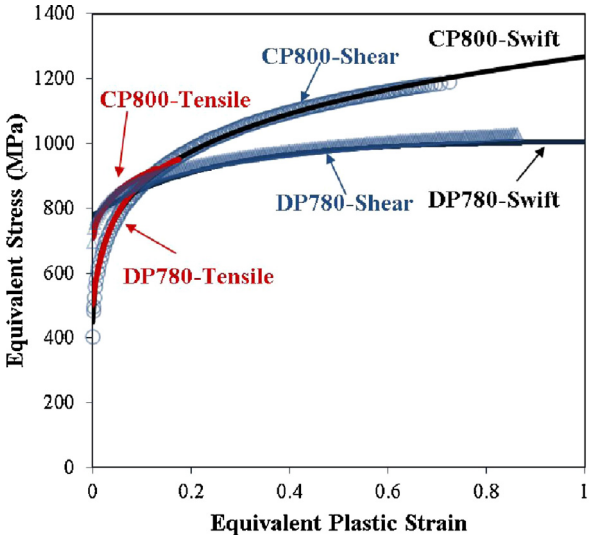

Fig. 8. The experimental true stress versus true plastic strain obtained from the tensile (RD) and shear tests for the two steels and the best fit curve based on Swift's hardening law.

Table 4
Swift's hardening law parameters.

Material	K	ε_o	n	R^2
CP800	1024	0.0067	0.07	0.99
DP780	1267	0.0018	0.16	0.98

The hardening behavior of the CP800 and DP780 materials was defined using the Swift law,

$$\sigma = K(\varepsilon o + \varepsilon^p)^n \tag{7}$$

where ε_o is the initial strain, ε^p is the plastic strain, and K and n are the material parameters that describe the rate of hardening. In conventional practice, Eq. (7) is fit to the true stress versus effective plastic strain response determined from uniaxial tensile samples; however the range of available hardening data prior to onset of necking is relatively low, as can be seen in Fig. 8. Instead, the calculated stress-ratios from the shear test, τ/σ_R (Table 2), was applied to extend the hardening curve using data from the shear experiments following the methodology described by Rahmaan et al. [50]. Fig. 8 shows the resulting hardening response as well as the Swift law fits (Table 4) which capture the measured data rather well.

3.2.2. Algorithm for stress integration from measured strains

The principal strains (ε_1,ε_2) under proportional loading can be expressed as,(ε_1,$\beta\varepsilon_1$), where β is a variable in the range [−1,1] that represents ratio of the plastic strain increments in the two principal directions. The stress ratio, α, is defined as the ratio of minor principal stress, σ_2, to major principal stress, σ_1. The strain ratios corresponding to stress ratios in the range $\alpha = [-2, 2]$ are determined using the Yld 91 yield function (Eq. (4)). For proportional loading, β is a constant that is defined by the normal to the yield surface at a particular stress ratio, α. To save computational time during the stress integration period, values of the stress ratios (α and $\gamma = \frac{\sigma_1}{\sigma}$) in the range $\alpha = [-2, 2]$ are tabulated along with the corresponding strain ratio determined using derivatives of the yield function. This range is selected to cover the stress states ranging from shear to biaxial tension to determine the typical stress ratios corresponding to strain paths in forming operations.

The plastic work increment is defined as, $dw^p = \sigma d\varepsilon^p$, where $d\varepsilon^p$ is the plastic strain increment

$$dw^p = \sigma d\varepsilon^p = \sigma_1 d\varepsilon_1 + \sigma_2 d\varepsilon_2 = (1+\alpha\beta)\sigma_1 d\varepsilon_1 \tag{8a}$$

Table 5
Average stress triaxiality (T) and Lode parameter (L) determined for biaxial tension, plane strain, uniaxial tension and simple shear deformation of the CP800 and DP780 steels.

Material	Biaxial tension		Plane strain		Uniaxial tension		Shear	
	T	L	T	L	T	L	T	L
CP800	0.66	0.97	0.55	−0.01	0.30	−0.92	0.00	0.01
DP780	0.66	0.98	0.55	0.01	0.30	−0.98	0.00	0.02

or

$$d\varepsilon^p = (1+\alpha\beta)\frac{\sigma_1}{\sigma}d\varepsilon_1 = (1+\alpha\beta)\gamma d\varepsilon_1, \text{where } \gamma = \frac{\sigma_1}{\sigma} \tag{8b}$$

The ε^p can be calculated by summing plastic strain increments. Using the hardening law, the equivalent stress, σ, corresponding to ε^pcan be determined.

The framework to determine stress-components from the major and minor strains is summarized as:

i Tabulate the values of $\beta = f(\alpha)$ and $\gamma = f(\alpha)$ using Yld91.
ii The strain ratio β_i is calculated at each experimental data point, i.
iii The stress ratios γ_i and α_i corresponding to β_i are determined from the database.
iv The equivalent plastic strain is calculated at each increment using Eq. (8b).
v The hardening law is updated to obtain the anisotropic equivalent stress, σ.
vi Major and minor stresses are calculated using γ_i, α_i i.e. $\sigma_1 = \gamma\sigma$ and $\sigma_2 = \alpha\sigma_1$.

3.3. Calculated stress triaxiality and Lode parameter

In this section, the evolution of equivalent plastic strain as a function of the stress triaxiality and the Lode parameter during the experiments is determined for plane stress conditions. To determine the stress states during deformation, the stress triaxiality and Lode parameter are determined using following equations

$$T = \frac{\sigma_m}{\sigma_{eq}} \tag{9}$$

$$L = -\frac{27}{2}\frac{(\sigma_1 - \sigma_m) * (\sigma_2 - \sigma_m) * (\sigma_3 - \sigma_m)}{\sigma_{eq}^3} \tag{10}$$

where $\sigma_m = \frac{\sigma_1 + \sigma_2 + \sigma_3}{3}$ is the mean stress and σ_{eq} is the von Mises effective stress. Figs. 9 and 10 show the equivalent strain as a function of stress triaxiality and Lode angle parameter, respectively, for the CP800 and DP780 samples during the biaxial dome, hole tension, v-bend and simple shear experiments. A constant stress-state is reported for the DP780 samples for all the stress states. The CP800 however exhibits non-linear stress triaxiality and Lode parameter for uniaxial tension and biaxial tension, while a linear trend is observed for shear and plane strain throughout the deformation. The average stress triaxiality and Lode parameter reported for both materials is indicated in Table 5 for all four loading conditions. It is important to state that for plane stress states, as assumed here in the analytical integration, the stress triaxiality and Lode parameter are not independent. As shown by Bai and Wierzbicki [58], only the triaxiality or the Lode parameter is sufficient to define the plane stress state.

4. Damage evolution under proportional loading

To systematically characterize damage accumulation, interrupted testing was conducted at four levels of displacement for the four different stress states: biaxial tension, uniaxial tension, plane-strain and simple shear. The four displacement levels were selected such that each

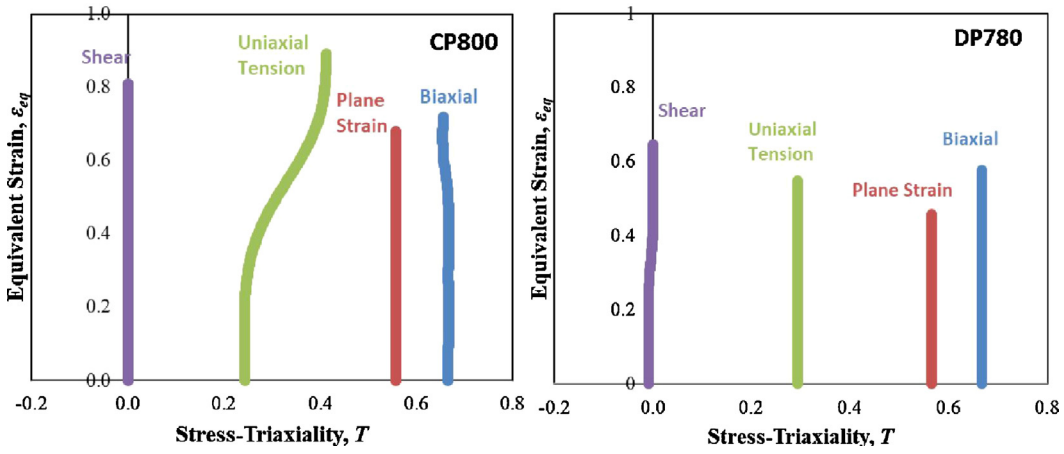

Fig. 9. Stress triaxiality history for biaxial tension, plane strain, uniaxial tension and shear deformation of the CP800 and DP780 steels.

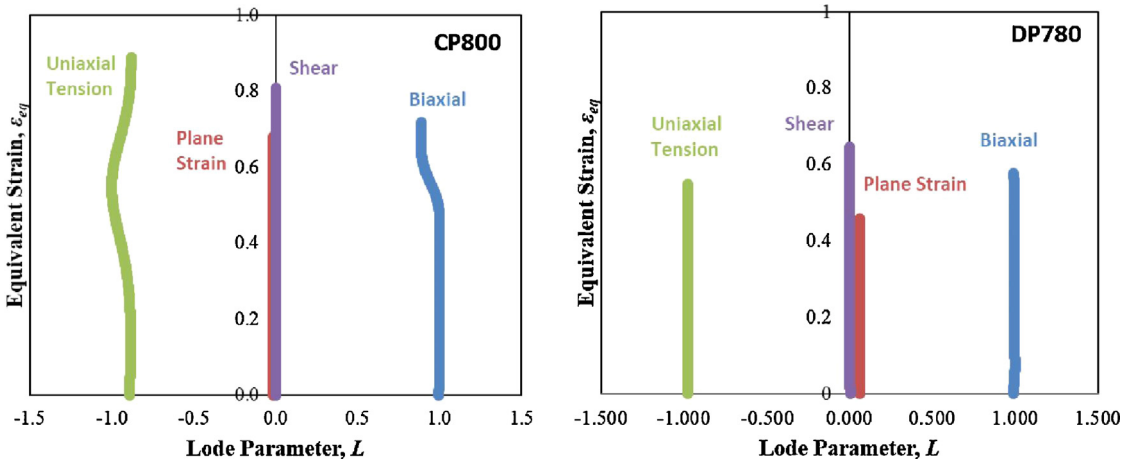

Fig. 10. Lode parameter history for biaxial tension, plane strain, uniaxial tension and shear deformation of the CP800 and DP780 steels.

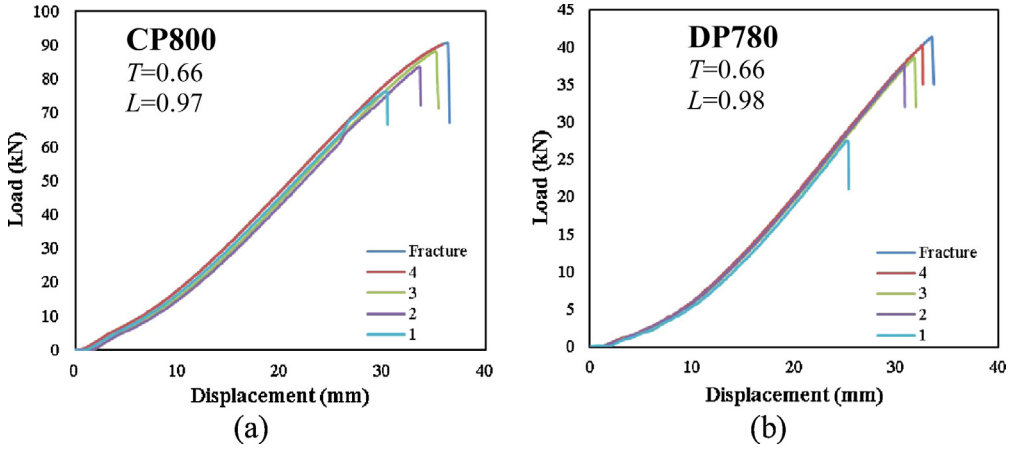

Fig. 11. Histories of load versus displacement strain for the (a) CP800 and (b) DP780 biaxial specimens interrupted at different strain levels.

specimen was deformed to approximately 50%, 70%, 85% and 95% of the failure strain. The load displacement response for the biaxial samples tested to failure as well as the interrupted samples that exhibit good repeatability up to the final strain level considered in each experiment is indicated in Fig. 11. The repeatability was similar for the other geometries (not shown for brevity).

3D tomography was performed on the interrupted specimens to quantify the number of voids nucleated at the different stages of deformation and loading conditions. The effect of stress state on void nucleation is discussed for the two materials, CP800 and DP780 steel, by comparing the number of voids nucleated (N) as a function of equivalent plastic strain (ε) for each loading condition.

The tomograms of the undeformed CP800 and DP780 steels are shown in Fig. 12 and the number of cavities per unit volume (N) measured for each specimen is specified.

4.1. Tomography

The tomographs acquired from the biaxial loaded samples interrupted at a Mises effective strain of 0.95% of the failure strain are shown

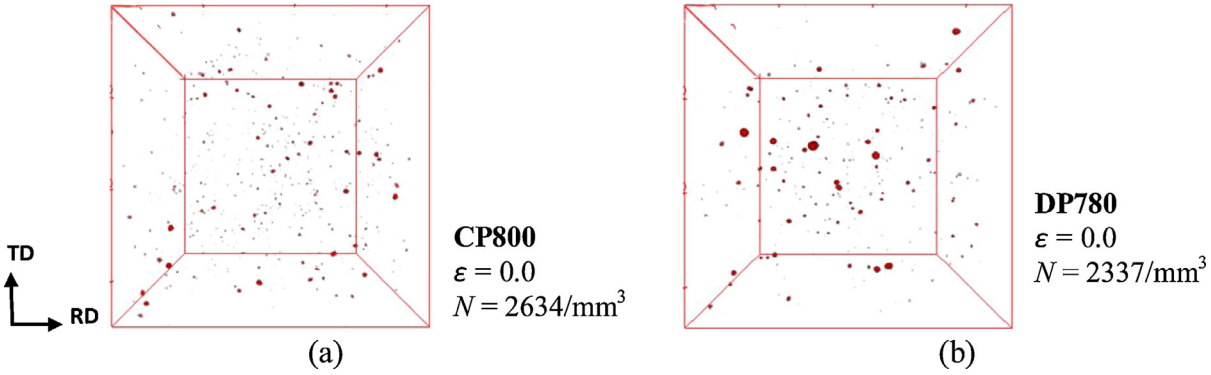

Fig. 12. 3D views of damage within the undeformed (a) CP800 and (b) DP780 specimen. The horizontal axis in the figure corresponds to the sheet RD while the vertical axis corresponds to the sheet TD.

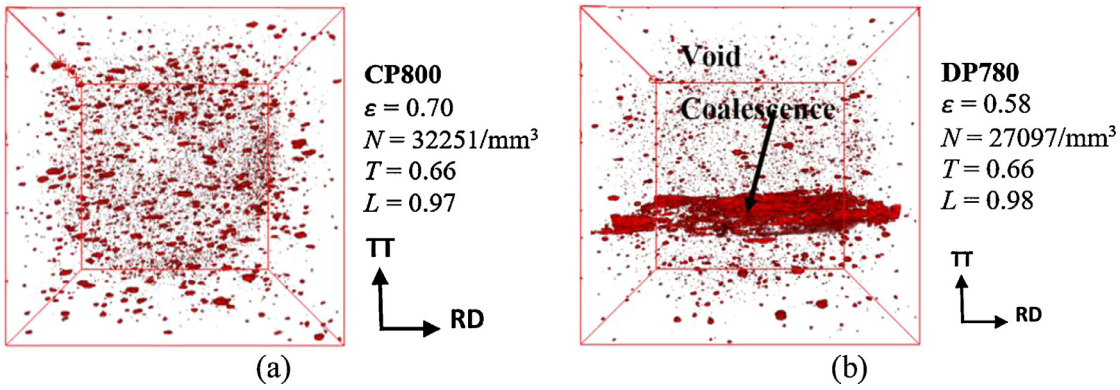

Fig. 13. 3D views of damage within the specimen deformed under biaxial tension loading near failure. The horizontal axis in the figure corresponds to the sheet RD while the vertical axis is the through-thickness (TT) direction.

in Fig. 13. The two biaxial loading directions corresponds to the rolling and transverse directions (RD and TD) and the tomographs are projected such that the plane of the figure corresponds to the sheet RD and through-thickness (TT) directions. The DP800 sample exhibits significant numbers of regions of local void coalescence that represents precursors to formation of macro-cracks. The DP780 sample exhibits extensive coalescence along the sheet mid-plane which corresponds to martensitic bands in the as-received sheet [7]. The number of cavities per unit volume (N) measured for each specimen is also indicated in Fig. 13.

Coalescence is generally favored along the ligament perpendicular to the loading direction and is difficult along ligaments which are not perpendicular to the loading direction [59]. Horstemeyer and Gokhale [60] demonstrated experimentally that under biaxial deformation the coalescence path is activated in two directions because the specimen is subjected to loading in the two directions and consequently the crack propagates along both directions. The plan-view projection of the coalescence plane indicated in Fig. 13 is shown in Fig. 14 and illustrates crack formation through coalescence of voids in the DP780 specimen deformed close to the failure strain. Since the DP780 specimen is deformed under a biaxial stress state, the void growth and subsequent coalescence occur in the two directions and consequently crack propagates along the two loading directions. This behavior could not be captured in the CP800 specimen because the experiment was terminated before the initiation of coalescence.

The hole tension specimens were loaded along the TD. The deformation of the reamed hole tension specimens follows uniaxial tension and the tomographs were acquired on the CP800 and DP780 reamed edges interrupted prior to fracture. Tomographs from the most deformed CP800 and DP780 specimens are shown in Fig. 15.

The comparison of the CP800 and DP780 tomograms deformed near failure (Fig. 15) suggests that the amount of damage developed near the failure strain is significantly higher in the CP800 specimen compared to the DP780 specimen. This difference in the damage evolution is attributed to the difference in microstructure of the two steels. The ferritic-bainitic CP800 microstructure can sustain deformation up to a larger strain due to lower strength-differential between the phases and exhibits more damage accumulation near the failure strain compared to the DP780 steel.

In contrast with the biaxial loading which exhibits void growth along the two loading directions, void growth is only significant in one direction under uniaxial tension, especially for the CP800 hole tension specimen. A similar trend was observed by Landron et al. [12] and Weck et al. [61] using 3D tomography As to be expected, in biaxial tension the voids will elongate in two directions that was also shown in the unit cell models of by Potirniche et al. [62]

Fig. 16 shows the damage during the deformation under plane-strain in the CP800 and DP780 plane strain v-bend specimens deformed to strains near failure. The void growth is not significant under plane-strain deformation. Pardoen and Brechet [63] reported two distinct coalescence mechanisms (1) internal necking of ligaments between voids and (2) internal shear localization involving limited void growth. Typically for plane strain specimens, ductility is less because a plane strain specimen is more susceptible to plastic shear localization due to the kinematic constraints [64]. A cluster of voids is however present in the vicinity of a crack (shown in Fig. 16) due to a high stress triaxiality. Consequently, the interaction of multiple voids along the crack front leads to crack growth and subsequent propagation of the crack.

For the shear specimens, the maximum deformation occurs at the center of the specimen due to rotation of the shear band as indicated

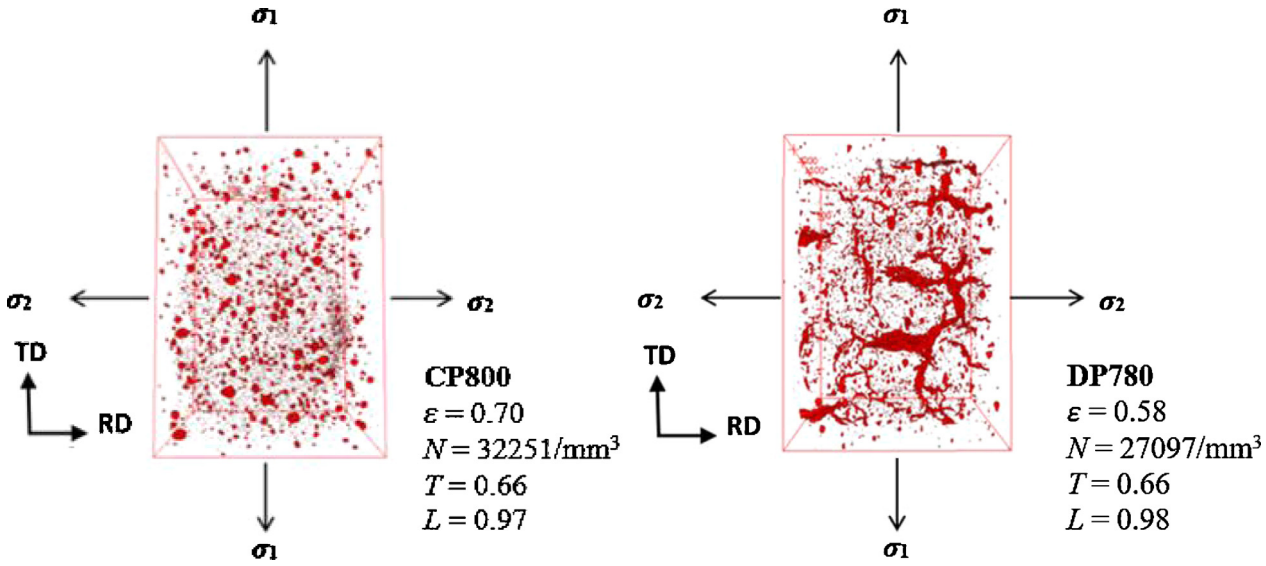

Fig. 14. 3D views of damage within the CP800 and DP780 specimens deformed under biaxial tension loading near failure. The horizontal axis in the figure corresponds to the sheet RD while the vertical axis is the transverse direction (TD).

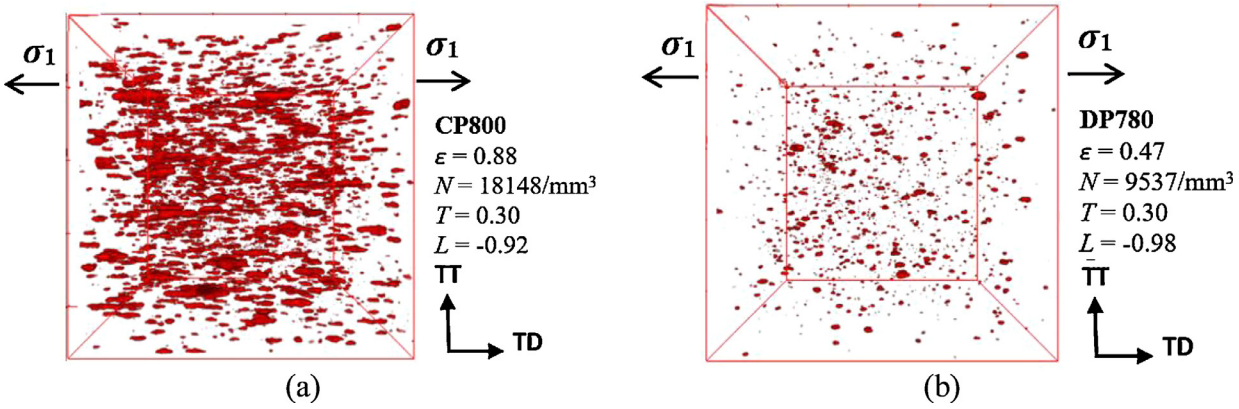

Fig. 15. 3D views of damage within the (a) CP800 and (b) DP780 hole tension specimens deformed near failure. The horizontal axis in the figure corresponds to the sheet TD while the vertical axis is the through-thickness (TT) direction.

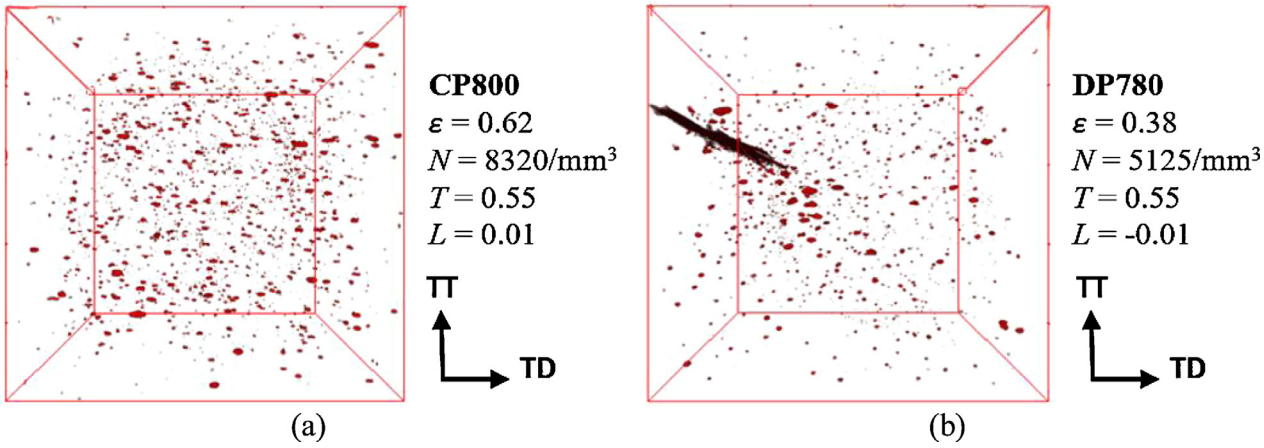

Fig. 16. 3D views of damage within the (a) CP800 and (b) DP780 specimens deformed under plane-strain loading at various steps of deformation. The horizontal axis in the figure corresponds to the sheet TD while the vertical axis is the through-thickness (TT) direction.

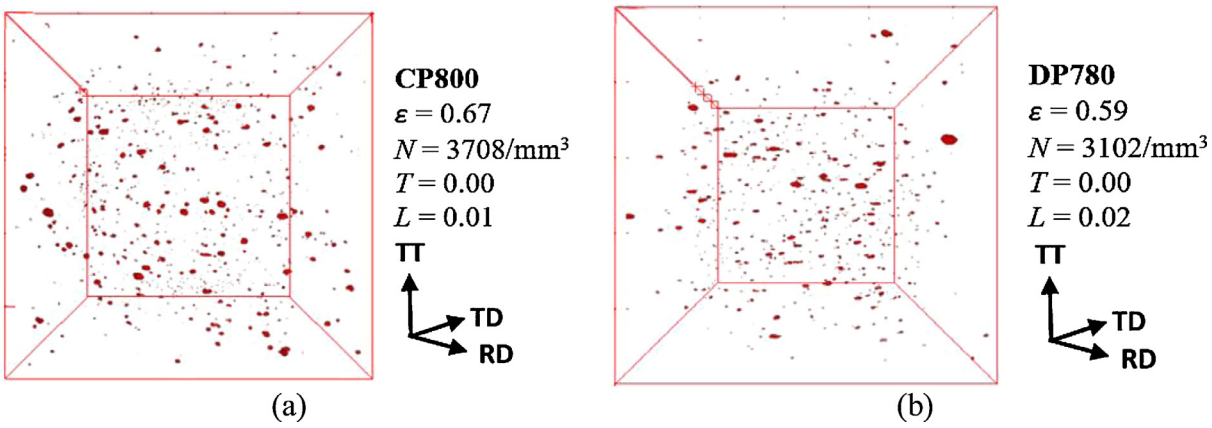

Fig. 17. 3D views of damage within the CP800 and DP780 specimens deformed under shear loading at various steps of deformation. The vertical axis in the figure corresponds to through-thickness (TT) direction while the horizontal axis is in the RD-TD plane.

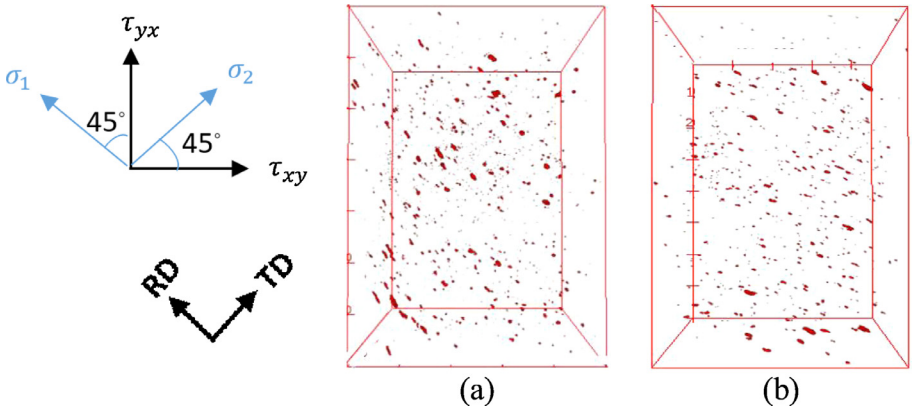

Fig. 18. 3D views of damage within the (a) CP800 and (b) DP780 specimens deformed under shear loading at near failure. The horizontal axis and vertical axis are aligned at 45° to the TD and RD respectively.

in the contour plots of the CP800 and DP780 steels (Fig. 5). The tomography specimen of cross-section 0.5 mm x 0.5 mm was therefore extracted from the center of the shear band of each interrupted specimen. Tomographs of the CP800 and DP780 shear specimens deformed to near failure are shown in Fig. 17. Void growth however is not significant during the shear loading of the DP780 and CP800 steels which is to be expected since due to absence of a hydrostatic stress to expand the void volume [22,59,65].

A second view or orientation of the tomographs for the most deformed shear specimens (Fig. 17) are shown in Fig. 18. For the simple shear loading type, normal stresses are almost negligible relative to the shear stress (τ_{xy}) so that principal plane is oriented 45° to the loading directions [49]. In the current shear loading condition, the location of principal stresses (σ_1 and σ_2) are aligned along the rolling and transverse directions and the shear stresses (τ_{xy}) are 45° to the rolling and transverse directions as indicated in Fig. 18. The voids have a tendency to rotate and align along the principal normal stresses and therefore are oriented along the rolling direction as shown in Fig. 18 for both the alloys.

4.2. Effect of loading condition on the damage evolution

Fig. 19 shows the number of voids nucleated as a function of equivalent strain for the different loading conditions. With an increase in equivalent strain, the extent of void nucleation increases for both the materials and all the stress-states. Void nucleation is a continuous process and the maximum nucleation rate occurred under biaxial tension and the minimum rate was in simple shear for both materials. The void density for the CP800 reamed edge under shear is 4000 per mm^3 at 0.7 strain while the void density under biaxial tension is eight times higher at 32,000 per mm^3. Void nucleation is clearly dependent upon the stress state for both materials. Similar results were observed by Landron et al. [11] and Needleman [19] which reported that the stress triaxiality has an impact on void nucleation rate.

The evolution of the porosity with the equivalent strain for the two materials subjected to different stress states is shown in Fig. 20. As deformation progresses, more voids are nucleated while the existing cavities grow and the void volume fraction increases. Since the number of nucleated voids and growth of voids under the plane-strain and shear stress states are less than that for biaxial tension and uniaxial tension at a given strain, the accumulation of damage is lower within the specimens subjected to shear and plane-strain loading for both the materials considered. This observation verifies that the damage accumulation is dependent upon the stress state for both materials.

5. Void nucleation model

The results presented in the previous section have demonstrated the influence of loading condition on the nucleation mechanism. To predict ductile failure accurately, the modeling of void nucleation is critical and therefore it is critical to account for the effect of stress state on the nucleation mechanism. In this section, modifications to the Chu and Needleman [36] nucleation models are presented to predict the nucleation process for a wide range of loading conditions using two criteria: strain-based and stress-based nucleation models. The efficacy of these two approaches is assessed.

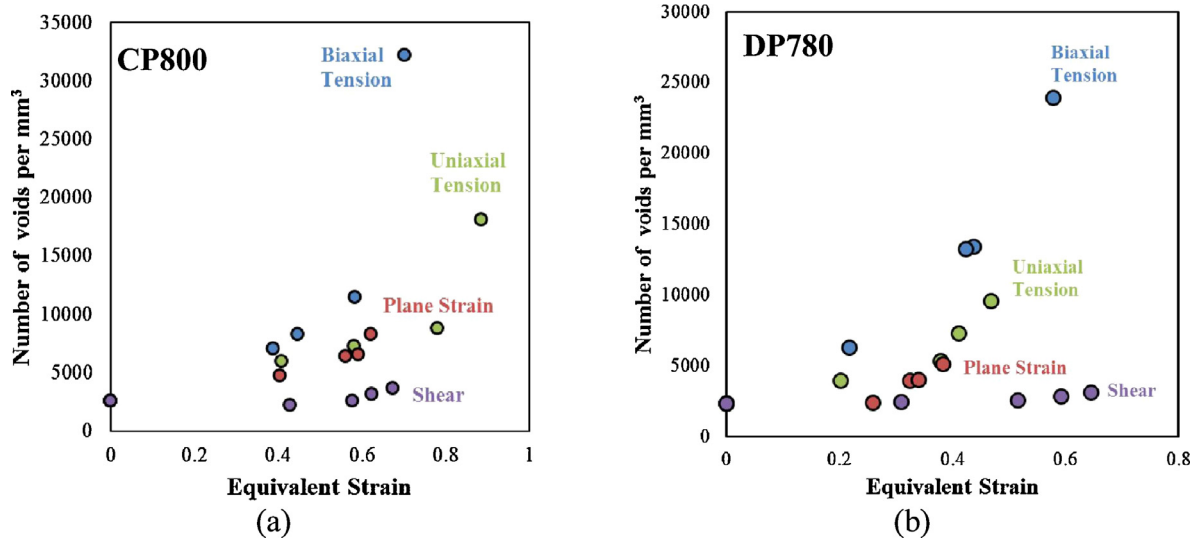

Fig. 19. Evolution of average void density with respect to equivalent strain for (a) CP800 and (b) DP780 steels.

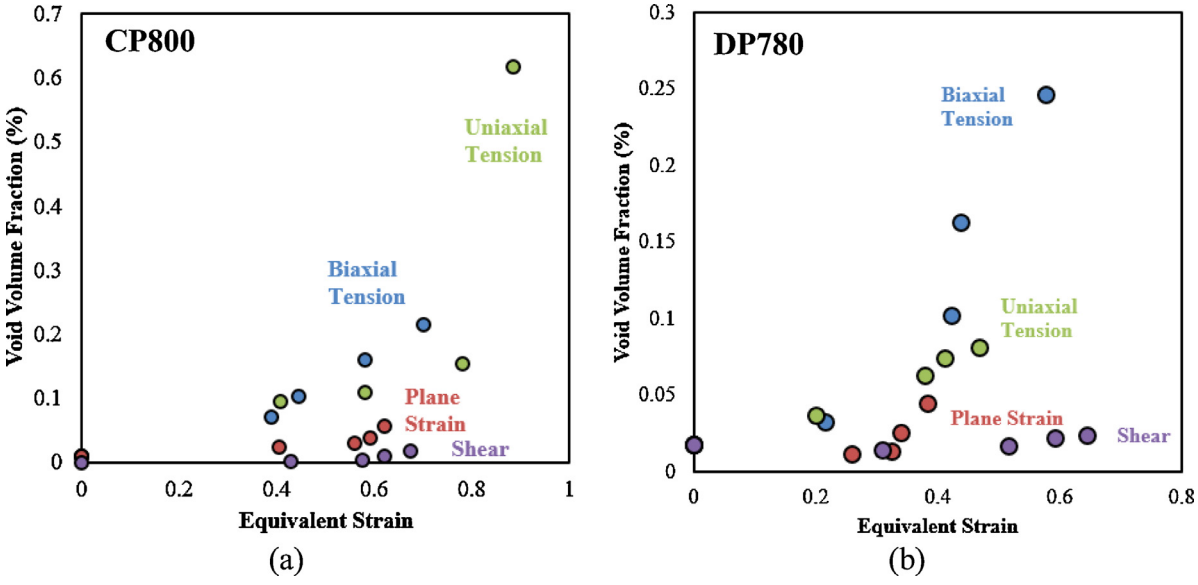

Fig. 20. Void volume fraction versus equivalent strain for (a) CP800 and (b) DP780.

5.1. Strain-based nucleation model

Chu and Needleman [36] postulated that the strain required to nucleate voids follows a normal distribution and can be expressed as:

$$\dot{N} = \frac{N_n}{s_N\sqrt{2\pi}} exp\left[\frac{-1}{2}\left(\frac{\varepsilon^p - \varepsilon_N}{s_N}\right)^2\right]\dot{\varepsilon}_p \tag{11a}$$

$$s_N = c_v * \varepsilon_N \tag{11b}$$

where N_n is the maximum number of voids per unit volume available to nucleate, $\dot{N}$ is the void nucleation rate, ε_N and s_N are the mean and standard deviation of the nucleation strain, c_v is the coefficient of variance of the nucleation strain and. N_n represents the number of potential void nucleation sites in a material and therefore is a material-dependent parameter. For a homogeneous material, N_n can be calculated from microstructural analysis of the volume fraction of second-phase particles and inclusions in the material. Chu and Needleman [36] and Søvik [66], assumed ε_N and s_N, to be material-specific parameters that were constant for all stress states. To assess the strain-controlled nucleation assumption, the predicted numbers of nucleated voids within CP800 based on a strain-controlled nucleation assumption (Eq. (11a)) was calculated using the following values of nucleation strain, ε_N = 1.0, 1.2, 1.4, 1.6, 1.8 and 2.0, an assumed value of c_v equal to 0.24 and s_N was calculated using Eq. (11b). N_n was used as 397,942 per mm^3 for CP800 (the value of N_n was calculated using the optimization approach described in Section 5.3). These predictions are plotted in Fig. 21, along with the observed number of voids per unit volume as a function of strain for the different stress state experiments on CP800. It is evident from the figure that the nucleation rates differ dramatically between stress states; therefore, the adoption of a simple strain-controlled nucleation model with ε_N, as a material parameter cannot predict the nucleation behavior for such a wide range of stress states. To capture the nucleation behavior for different stress states, ε_N could be determined individually for each loading condition, but such an approach has not been investigated thus far.

5.2. Stress-based nucleation model

Nucleation rules based on critical stress and stress concentrations are available in the literature [41,35,67]. For practical applications, the

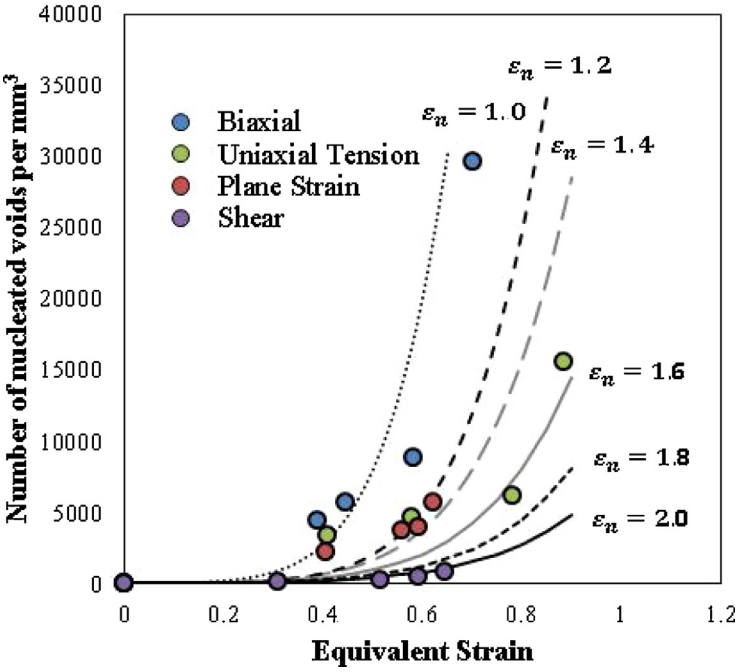

Fig. 21. Predictions using Chu and Needleman's strain-based nucleation rule for CP800 using various nucleation strain assumptions. Solid curves are predictions using Eq. (11), while symbols are measurements from interrupted samples.

stress-based Chu and Needleman [36] nucleation criterion has been used extensively in past work [39,68,69] and can be expressed as

$$\dot{N} = \frac{N_n}{s_n\sqrt{2\pi}} \exp\left[\frac{-1}{2}\left(\frac{\sigma_n - \sigma_N}{s_n}\right)^2\right]\dot{\sigma}_n \tag{12a}$$

$$s_n = C_v * \sigma_N \tag{12b}$$

where σ_n is the nucleation stress, σ_N and s_n are the average and standard deviation of the nucleation stress and C_v is the coefficient of variance of the nucleation stress. Fowler et al. [68] examined Argon's nucleation stress criterion to estimate nucleation stress for Chu and Needleman's stress-controlled nucleation model and reported that the stress-controlled nucleation model can captures the experimentally observed dependence of nucleation strain on stress triaxiality. Shabrov and Needleman [70] extended Argon's criterion that relates the nucleation stress to the stress in the matrix material as given by the following relation:

$$\sigma_n = c\sigma_{eq} + \sigma_{hyd} \text{ where } \sigma_{hyd} = \frac{\sigma_1 + \sigma_2 + \sigma_3}{3} \tag{13}$$

For periodically distributed particles, $c \approx 0.44$ for cubic particles and $c \approx 0.35$ for spherical particles [70]. To illustrate the use of a stress-controlled nucleation criterion, Similar to the strain-controlled nucleation model, N_n and C_v are considered material-specific properties and held constant for all the loading conditions. C_v was taken as 0.04 and 0.10 for the CP800 and DP780 steels respectively. The stress components, unlike the strain components, cannot be obtained from experiments and the stress integrator described in Section 3 is used to determine stress components (σ_1,σ_2) from the strain components (ε_1,ε_2) derived from the experimental data. The predicted nucleation response is plotted in Fig. 22, along with the measured data from the interrupted samples. With σ_N = 1070 and 746 MPa, the predicted nucleation mechanism agrees with the measured values only for the biaxial stress state and uniaxial tension loading, respectively. The predicted number of nucleated voids for the other stress states is either higher compared to the measured value or lower. This observation suggests that despite the stress-based nucleation model being dependent on the stress triaxiality, the adoption of single σ_N to predict nucleation for all the stress states is not achievable using the current definition of the nucleation stress of Eq. (13) that is based upon particle debonding. It is possible that other forms for the nucleation stress such as that of Beremin [35] could provide a better description.

5.3. Introduction of Lode-dependence of nucleation strain

The major limitation of Chu and Needleman's nucleation model is that it does not fully account for the effect of stress state. The experimental results presented in Section 4 and the work done by [11] suggests that the nucleation mechanism varies with the loading condition. To account for this behavior, a modification to Chu and Needleman's criteria is proposed in which nucleation strain becomes a function of both stress triaxiality and Lode parameter. In the light of the proposed dependency of nucleation mechanism on stress state, the nucleation strain, ε_N, was first determined individually for each loading condition as a function of stress triaxiality as well as Lode parameter, and the modified nucleation model is expressed in following equation.

$$\dot{N} = \frac{N_n}{s_N\sqrt{2\pi}} exp\left[\frac{-1}{2}\left(\frac{\varepsilon_p - \varepsilon_N(T,L)}{s_N}\right)^2\right]\dot{\varepsilon}_p \tag{14}$$

As before, N_n and C_v are considered to be constant for all the stress states.

An optimization code was written in MATLAB to determine the parameters in Eq. (14) for both steels, using an assumed normal distribution of the observed void density versus strain data for the different stress states. The global optimization MATLAB subroutine based on genetic algorithm, was used to minimize error between the values predicted by the nucleation model and the experimental data points. The Error function was defined as:

$$Error = \sum_{i=1}^{4} w_i\left(\left(\frac{N_{model}}{N_{exp}}\right)_i - 1\right)^2 \tag{15}$$

where the "exp" and "model" indicate experimental values and predicted nucleated void density respectively, from the nucleation model. w_i are weighting parameters for the number of experimental data points where $i = 1$ corresponds to experimental data point acquired at the lowest strain, $i = 2$, the data point obtained at the next strain level, and so on. In the present work, the weighting parameters were assigned in such a manner that a higher weighting is given to the experimental data points acquired at a higher strain level i.e. w_1 = 0.125, w_2 = 0.25, w_3 = 0.5,

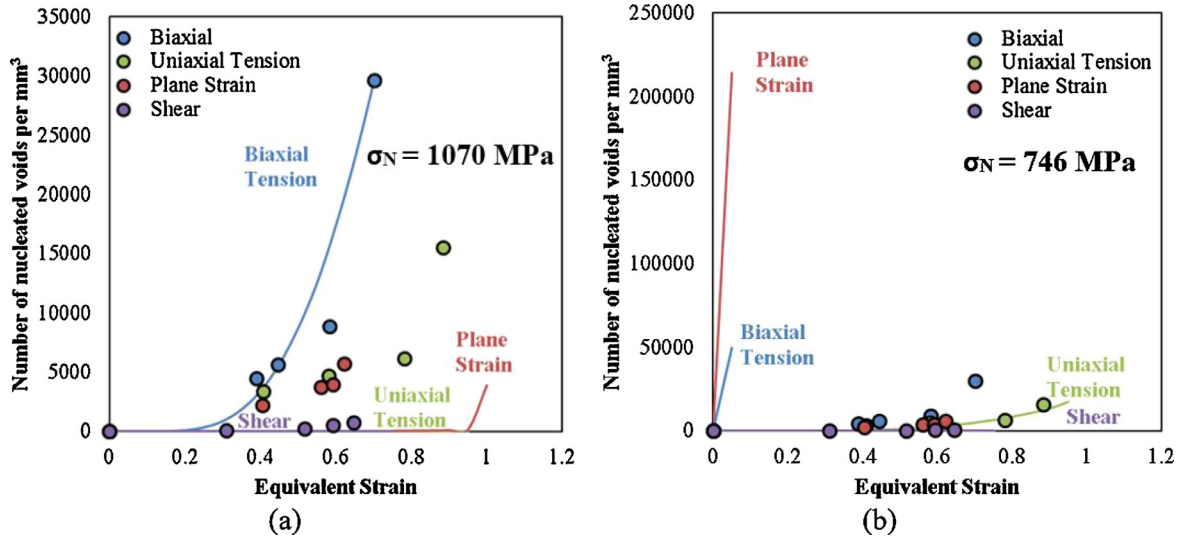

Fig. 22. Predictions using Chu and Needleman's stress-based nucleation rule using various assumed nucleation stress levels: (a) 1070 MPa and (b) 746 MPa. Solid curves are predictions using Eq. (12), while symbols are measurements from interrupted samples.

Table 6
Nucleation parameters for the different stress states of the CP800 and DP780 steels.

Material	N_n (per mm^3)	c_v	Biaxial tension			Plane strain			Uniaxial tension			Shear		
			ϵ_N	T	L	ϵ_N	T	L	ϵ_N	T	L	ϵ_N	T	L
CP800	397,942	0.24	1.10	0.66	0.97	1.34	0.55	−0.01	1.58	0.30	−0.92	2.20	0.00	0.02
DP780	48,000	0.31	0.50	0.66	0.98	0.80	0.55	0.01	0.70	0.30	−0.98	1.40	0.00	0.01

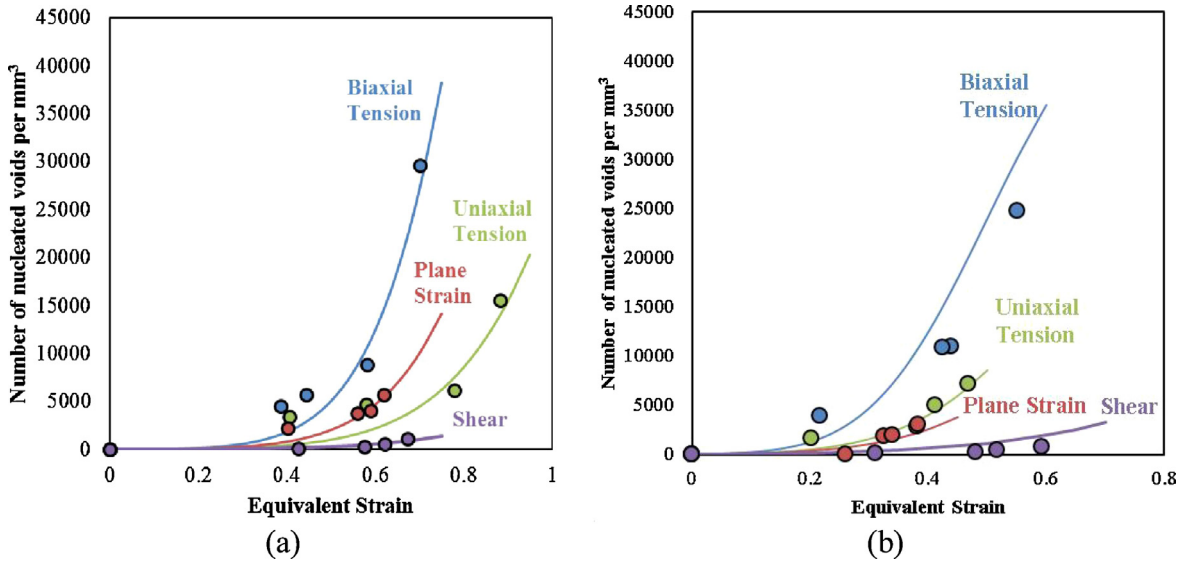

Fig. 23. The implementation of Lode parameter-dependent strain-based Chu and Needleman nucleation rule using Eq. (14) for the various loading conditions of the (a) CP800 and (b) DP780 steels. Solid curves are predictions using Eq. (14), while symbols are measurements from interrupted samples.

$w_4 = 1$ (recall that four tomography images (data points) were acquired for each stress state). The nucleation parameters determined for each loading condition using the optimization approach described above are listed in Table 6 for the CP800 and DP780 steels. The resulting nucleation predictions are shown in Fig. 23 from which it can be seen that the model predictions capture the trends in the measured data rather well.

The nucleation parameters listed in Table 6 predict the nucleation rates for the specific stress states corresponding to the measured damage histories. To develop a more comprehensive expression to predict nucleation under different loading conditions, a functional dependence of average nucleation strain on both stress triaxiality and Lode parameter is introduced. In this case, the functional form of the fracture *locus* proposed by Bai and Wierzbicki [58] is adopted to develop a "nucleation strain surface" that can be expressed as:

$$\epsilon_N = \left\{ \frac{C_1}{C_2}\left[C_3 + \frac{\sqrt{3}}{2-\sqrt{3}}(1 - C_3)\left(\sec\left(\frac{\pi L}{6}\right) - 1\right)\right] \times \left[\sqrt{\frac{1+C_4^2}{3}}\cos\left(\frac{\pi L}{6}\right) + C_4\left(T + \frac{1}{3}\sin\left(\frac{\pi L}{6}\right)\right)\right]\right\}^{\frac{-1}{C_5}} \tag{16}$$

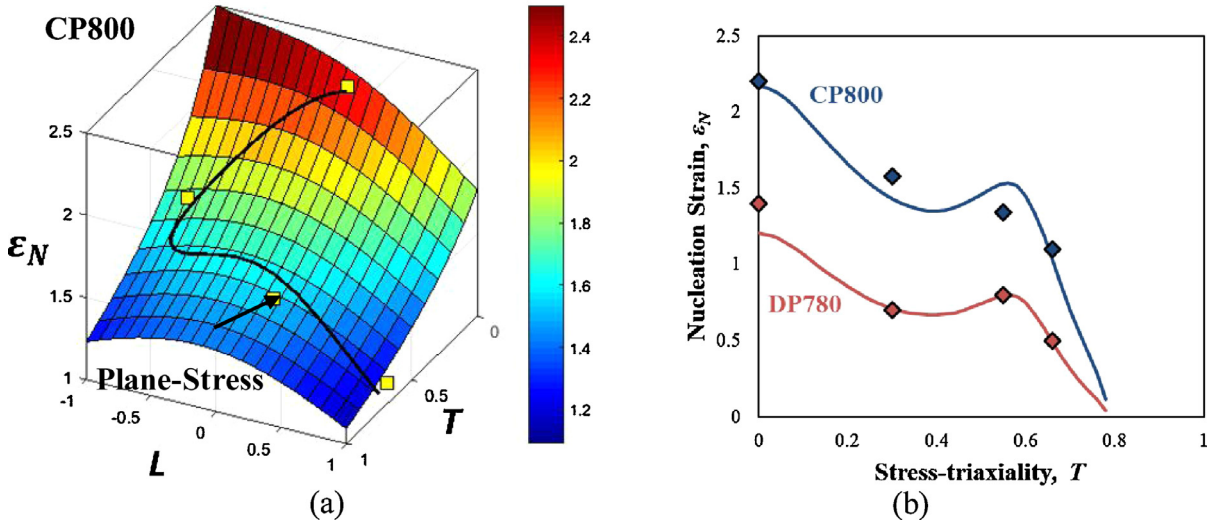

Fig. 24. (a) Representation of nucleation strain (ε_N) surface as a function stress triaxiality (T) and Lode angle parameter (L) for the CP800 steel. (b) The plane stress curve locus corresponding to the stress states and experimental data points are indicated by black line and square symbols, respectively.

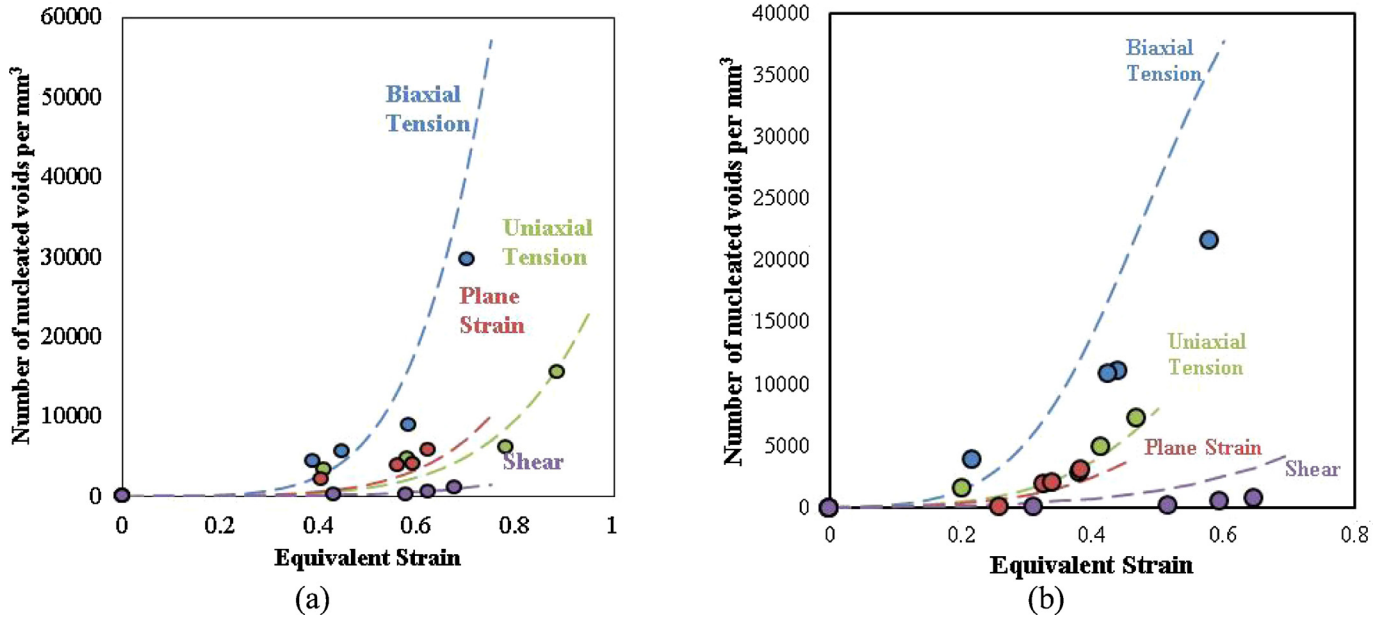

Fig. 25. Predicted nucleated voids as a function of equivalent strain for the various loading conditions of the (a) CP800 and (b) DP780 steels. Solid curves are predictions using Eq. (14), while symbols are measurements from interrupted samples.

Table 7
Material parameters for the CP800 and DP780 steels listed in Eq. (16) and Error in Eq. (17).

Material	C_1	C_2	C_3	C_4	C_5	Error
CP800	0.44	1.7	0.7	2.2	1.8	0.03
DP780	1.80	901.5	0.7	1409.0	1.7	0.02

where C_{1-5} are material parameters and are listed in Table 7 for the two steels. Note that c_v is independent of loading condition, as is N_n. The constants in Eq. (16) were identified using the genetic algorithm in MATLAB. Although the formulation shown in Eq. (16) has five coefficients, the number of coefficients can be reduced to four by replacing C_1/C_2 with a single variable. Subsequently, the four coefficients values can be determined by plugging in the four sets of experimental values. The error between the values predicted by the nucleation model and the experimental data points was minimized using the Error function defined as

$$Error = \sum_{i=1}^{4} w_i \left(\left(\frac{\varepsilon_{model}}{\varepsilon_{exp}} \right)_i - 1 \right)^2 \tag{17}$$

Where "exp" and "model" indicate experimental values and predicted nucleated void density respectively, from the nucleation model. w_i are weighting parameters for the four loading conditions and assumed to be unity for all the cases to provide equal weightage to all the stress-states.

Fig. 24 shows the resulting nucleation surfaces for the two steels that cover a broad range of stress states. Also shown is the so-called plane stress locus corresponding to the stress states accessed in the current experiments (symbols). The nucleation rate for a given stress state can then be predicted by substituting the nucleation strain, from Eq. (16), corresponding to the loading condition, into Chu and Needleman's nucleation criterion of Eq. (14) along with the respective material parameters, N_n and c_v. The predicted void density as a function of equivalent

strain for the various loading conditions are shown in Fig. 25 along with the experimental data.

6. Conclusions

1 The rate of damage nucleation is lower for the CP800 steel relative to DP780. This difference can be attributed to the lower strength differential between phases of the ferritic-bainitic CP800 steel [7], leading to a higher nucleation strain and rapid nucleation of voids in comparison to the ferritic-martensitic DP780 steel.
2 The influence of stress state, in terms of triaxiality and Lode parameter, on nucleation behavior was characterized for the DP780 and CP800 steel sheet. At a given strain, the number of voids per unit volume observed during the biaxial dome test was highest while the void nucleation was lowest under simple shear deformation for both materials considered.
3 Strain-based or stress-based nucleation criteria alone were unable to capture the measured dependency of nucleation rate on stress-state. The introduction of Lode parameter-dependency of nucleation rate, in addition to stress-triaxiality, accurately captured the measured nucleation behavior. The use of a nucleation surface will enable application to three-dimensional stress states and will be evaluated in future work.

Declaration of Competing Interest

The authors declare that they have no known competing financial interests or personal relationships that could have appeared to influence the work reported in this paper.

CRediT authorship contribution statement

N. Pathak: Conceptualization, Data curation, Methodology, Writing - original draft, Writing - review & editing. **J. Adrien:** Data curation, Writing - review & editing. **C. Butcher:** Conceptualization, Methodology, Writing - original draft, Writing - review & editing. **E. Maire:** Data curation, Writing - review & editing. **M. Worswick:** Conceptualization, Methodology, Writing - original draft, Writing - review & editing.

Acknowledgments

This work was funded by the AUTO21 Network of Centers of Excellence, the Natural Sciences and Engineering Research Council of Canada (NSERC), the Ontario Research Fund, and the Canada Research Chairs Secretariat. The authors would also like to acknowledge the assistance of their industrial partner, ArcelorMittal Dofasco. The authors would like to thank Armin Abedini for his help in calibrating yield function.

References

[1] Billur T, Altan T. Challenges in forming advanced high strength steels. Proc New Dev Sheet Metal Form 2012:285–304.
[2] Takuda H, Mori K, Fujimoto H, Hatta N. Prediction of forming limit in bore-expanding of sheet metals using ductile fracture criterion. J Mater Process Technol 2011;92-93:433–8.
[3] J. Dykeman, S. Malcolm, B. Yan, J. Chintamani, G. Huang, N. Ramietti and H. Zhu, "Characterization of edge fracture in various types of advanced high strength steel," *SAE Technical Paper* 2011-01-1058, 2011.
[4] Hasegawa K, Kawamura K, Urabe T, Hosa Y. Effects of microstructure on stretch-flange-formability of 980 MPa Grade cold-rolled ultra high strength steel sheets. ISIJ Int 2004;44(3):603–9.
[5] Sudo M, Hashimoto S, Kambe S. Niobium bearing ferrite-bainite high strength hot-rolled sheet steel with improved formability. Trans Iron Steel Inst Jpn 1983;23(4):303–11.
[6] Pathak N, Butcher C, Worswick M. Assessment of the critical parameters influencing the edge stretchability of advanced high strength steel. J Mater Eng Perform 2016;25(11).
[7] Pathak N, Butcher C, Worswick M, Bellhouse E, Gao J. Damage evolution in complex-phase and dual-phase steels during edge stretching. Materials (Basel) 2017;10(4):346.
[8] Kanetake N, Nomura M, Choh T. Continuous observation of microstructural degradation during tensile loading of particle reinforced aluminum composites. Mater Sci Technol 1995;11:1246–52.
[9] Benzerga A, Leblond J. Effective yield criterion accounting for microvoid coalescence. J Appl Mech 2014;81(3):031009.
[10] Avramovic-Cingara G, Ososkov Y, Jain M, Wilkinson D. Effect of martensite distribution on damage behaviour in DP600 dual phase steels. Mater Sci Eng 2009;516(1):7–16.
[11] Landron C, Bouaziz O, Maire E, Adrien J. Characterization and modeling of void nucleation by interface decohesion in dual phase steels. Scr Mater 2010;63(10):973–6.
[12] Landron C, Maire E, Bouaziz O, Adrien J, Lecarme L, Bareggi A. Validation of void growth models using X-ray microtomography characterization of damage in dual phase steels. Acta Mater 2011;59(20):7564–73.
[13] Landron C, Bouaziz O, Maire E, Adrien J. Experimental investigation of void coalescence in a dual phase steel using X-ray tomography. Acta Mater 2013;61(18):6821–9.
[14] Kahziz M, Morgeneyer T, Maziere M, Maire E, Bouaziz O. 3D synchrotron laminography assessment of damage evolution in blanked dual phase steels. 13th international conference on fracture; 2013.
[15] Pardoen T, Hutchinson J. An extended model for void growth and coalescence. J Mech Phys Solids 2000;48(12):2467–512.
[16] Dunand M, Mohr D. Effect of Lode parameter on plastic flow localization after proportional loading at low stress triaxialities. J Mech Phys Solids 2014;66:133–53.
[17] Hancock J, Mackenzie A. On the mechanisms of ductile failure in high-strength steels subjected to multi-axial stress-states. J Mech Phys Solids 1976;24:147–69.
[18] Barsoum I, Faleskog J. Rupture mechanisms in combined tension and shear—experiments. Int J Solids Struct 2007;44(6):1768–86.
[19] Needleman A. Continuum model for void nucleation by inclusion debonding. Journal of. J Appl Mech 1987;54:525–31.
[20] Xu X, Needleman A. Numerical simulations of fast crack growth in brittle solids. J Mech Phys Solids 1994;42(9):1397–434.
[21] Yu Q. Influence of the stress state on void nucleation and subsequent growth around inclusion in ductile material. Int J Fract 2015;193(1):43–57.
[22] Rice J, Tracey D. On the ductile enlargement of voids in triaxial stress fields. J Mech Phys Solids 1969;17(3):201–17.
[23] Thomason P. Ductile spallation fracture and the mechanics of void growth and coalescence under shock-loading conditions. Acta Mater 1999;47(13):3633–46.
[24] Erdogan M. The effect of new ferrite content on the tensile fracture behaviour of dual phase steels. J Mater Sci 2002;37(17):3623–30.
[25] Thomason P. Ductile fracture of metals. Oxford: Pergamon Press; 1990.
[26] McClintock F. A criterion for ductile fracture by the growth of holes. J Appl Mech 1968;35:363–71.
[27] Lassance D, Scheyvaerts F, Pardoen T. Growth and coalescence of penny-shaped voids in metallic alloys. Eng Fract Mech 2006;73:1009–34.
[28] Babout L, Br´echet Y, Maire E, Foug'eres R. On the competition between particle fracture and particle decohesion in metal matrix composites. Acta Mater 2004;52:4517–25.
[29] Thomson C, Worswick M, Pilkey A, Lloyd D, Burger G. Modeling void nucleation and growth within periodic clusters of particles. J Mech Phys Solids 1998;47(1):1–26.
[30] Ghadbeigi H, Pinna C, Celottob S. Failure mechanisms in DP600 steel: initiation, evolution and fracture. Mater Sci Eng 2013;588:420–31.
[31] Ahmad E, Manzoor T, Ali K, Akhter J. Effect of microvoid formation on the tensile properties of dual-phase steel. J Mater Eng Perform 2000;9(3):306–10.
[32] Khodabakhshia F, Haghshenasb M, Eska H. Hardness–strength relationships in fine and ultra-fine grained metals processed through constrained groove pressing. Mater Sci Eng 2015;636:331–9.
[33] Tanaka K, Mori T, Nakamura T. Cavity formation at the interface of a spherical inclusion in a plastically deformed matrix. Philos Mag 1970;21(170):267–79.
[34] Argon A, Im J, Needleman A. Distribution of plastic strain and negative pressure in necked steel and copper bars. Metall Trans 1975;6A:815–24.
[35] Beremin F. Cavity formation from inclusions in ductile fracture of A50S steel. Metall Trans 1981;12(A):723–31.
[36] Chu C, Needleman A. Void nucleation effects in biaxially stretched sheets. J Eng-Mater Technol 1980;102:249–56.
[37] Chen Z, Worswick M. Investigation of void nucleation in Al-Mg sheet. Mater Sci Eng 2008;484-484:99–101.
[38] Nahshon K, Xue Z. A modified Gurson model and its application to punch-out experiments. Eng Fract Mech 2009;76(8):997–1009.
[39] Butcher C, Chen Z, Worswick M. A lower bound damage-based finite element simulation of stretch flange forming of Al-Mg alloys. Int J Fract 2006;142:289–98.
[40] Butcher C, Chen Z, Bardelcik A, Worswick M. Damage-based finite-element modeling of tube hydroforming. Int J Fract 2009;155:55–65.
[41] Argon A, Im J, Safoglu R. Cavity formation from inclusions in ductile fracture. Metall Trans 1975;6A:825–37.
[42] Barlat F, Lege D, Brem J. A six-component yield function for anisotropic materials. Int J Plast 1991;7(7):693–712.
[43] Nakazima K, Kikuma T, Hasuka K. Study on the formability of steel sheets. Yawata Iron and Steel Publications; 1968.
[44] Ebnoether F, Mohr D. Predicting ductile fracture of low carbon steel sheets: stress-based versus mixed stress/strain-based Mohr–Coulomb model. Int J Solids Struct 2013;50(7):1055–66.
[45] Bao Y, Wierzbicki T. On fracture locus in the equivalent strain and stress triaxiality space. Int J Mech Sci 2004;46(1):81–98.
[46] Cheong K, Omer K, Butcher C, George R, Dykeman J. Evaluation of the VDA 238-100 Tight Radius Bending Test using Digital Image Correlation Strain Measurement. International deep drawing conference Munich; 2017.

[47] “VDA 238-100 test specification draft: Platebending test for metallic materials,” 12/2010, 2017
[48] Peirs J, Verleysen P, Degrieck J. Novel technique for static and dynamic shear testing of Ti6Al4V sheet. Exp Mech 2012;52:729–41.
[49] Abedini A, Butcher C, Worswick M. Fracture characterization of rolled sheet alloys in shear loading: studies of specimen geometry, anisotropy, and rate sensitivity. J Exp Mech 2016;57(1):75–88.
[50] Rahmaan T, Abedini A, Butcher C, Pathak N, Worswick M. Investigation into the shearstress, localization and fracture behavior of DP600 and AA5182-O sheet metal alloys under elevated strain rates. Int J Impact Eng 2017;108:303–21.
[51] Abràmoff M, Magalhães P, Ram S. Image processing with ImageJ. Biophoton Int 2004;11(7):36–42.
[52] Landron C, Maire E, Adrien J, Bouaziz O, Di Michiel M, Cloetens P, Suhonen H. Resolution effect on the study of ductile damage using synchrotron X-ray tomography. Nucl Instrum Methods Phys Res, Sect B 2012;284:15–18.
[53] Jonas J, Ghosh C, Basabe V, Shrivastava S. The Hencky equivalent strain ant its inapplicability to the interpretation of torsion testing experiments. Philos Mag 2012;92:2313–28.
[54] Shrivastava S, Ghosh C, Jonas J. A comparison of the von Mises and Hencky equivalent strains for use in simple shear experiments. Philos Mag 2012;92:779–86.
[55] Butcher C, Abedini A. Shear confusion: identification of the appropriate equivalent strain in simple shear using the logarithmic strain measure. Int J Mech Sci 2017;134:273–83.
[56] Roth C, Mohr D. Ductile fracture experiments with locally proportional loading histories. Int J Plast 2016;79:328–54.
[57] Abedini A, Butcher C, Rahmaan T, Worswick M. Evaluation and calibration of anisotropic yield criteria in shear Loading: constraints to eliminate numerical artefacts. Int J Solids Struct 2017;151:118–34.
[58] Bai Y, Wierzbicki T. A new model of metal plasticity and fracture with pressure and Lode dependence. Int J Plast 2008;24(6):1071–96.
[59] Benzerga A, Leblond J. Ductile fracture by void growth to coalescence. Adv Appl Mech 2010;44:169–305.
[60] Horstemeye M, Gokhale AM. A void-crack nucleation model for ductile metals. Int J Solids Struct 1999;36:5029–55.
[61] Weck A, Wilkinson D, Maire E, Toda H. Visualization by X-ray tomography of void growth and coalescence leading to fracture in model materials. Acta Mater 2008;56(12):2919–28.
[62] Potirniche G, Hearndon J, Horstemey M, Ling X. Lattice orientation effects on void growth and coalescence in fcc single crystals. Int J Plast 2006;22(5):921–42.
[63] Pardoen T, Brechet Y. Influence of microstructure-driven strain localization on the ductile fracture of metallic alloys. Philos Mag 2004;84:269–97.
[64] Scheyvaertsa F, Onck P, Tekog˙lua C, Pardoen T. The growth and coalescence of ellipsoidal voids in plane strain under combined shear and tension. J Mech Phys Solids 2011;59(2):373–97.
[65] Fleck N, Hutchinson J. Void growth in shear. Proc R Soc Lond A 1986;407(1833).
[66] Søvik O. Experimental and numerical investigation of void nucleation in an AlMgSi alloy. Le Journal de Physique IV 1996;6(C6) C6-155-C6-164.
[67] Lee B, Mear M. Axisymmetric deformation of power–law solids containing a dilute concentration of aligned spheroidal voids. J Mech Phys Solids 1992;40:1805–36.
[68] Fowler J, Worswick M, Pilkey A, Nahme H. Damage leading to ductile fracture under high strain-rate conditions. Metall Mater Trans A 2000;31(3):831–44.
[69] Lassance D, Scheyvaerts F, Pardoen T. Growth and coalescence of penny-shaped voids in metallic alloys. Engineering Fracture Mechanics. Eng Fract Mech 2006;73:1009–34.
[70] Shabrov M, Needleman A. An analysis of inclusion morphology effects on void nucleation. Model Simul Mater Sci Eng 2002;10(2):162.